PEOPLE'S DEMOCRATIC REPUBLIC OF ALGERIA

MINISTRY OF HIGHER EDUCATION AND SCIENTIFIC RESEARCH

UNIVERSITY YAHIA FARES OF MEDEA

Faculty of Technology

Department of Mechanical Engineering



Master's Thesis

Modélisation et simulation des défauts de cassure de barres dans la MAS à Cage

Field: Electromechanics

Specialty: Electromechanics

Presented by:

ZIAINIA Mohamed El Amine

Proposed and supervised by:

Dr. BERRAHAL khoukha

2024/2025

Acknowledgments

In the name of Allah, the Most Compassionate, the Most Merciful, I begin by expressing my profound gratitude to Almighty God for granting me the strength, health, and patience throughout my academic journey. Without His blessings, the completion of this paper would not have been possible.

I extend my heartfelt thanks to my supervisor, Dr. **BERRAHAL Khoukha**, whose patience, availability, and insightful guidance have been invaluable in shaping the direction and quality of my research.

My sincere appreciation goes to the distinguished members of my thesis committee Jury President Professor **HANINI Noureddine** and examiner Dr. **REBHI Redha** whose thoughtful feedback and rigorous evaluation have been essential in refining my study.

I am forever indebted to my family for their unwavering encouragement and understanding throughout my academic pursuits. Their love and belief in me have been a constant source of inspiration and motivation.

Finally, I wish to thank all those who have supported me in various ways during this journey. This thesis stands not only as a testament to my individual efforts but also as a reflection of the collective support and dedication of everyone who has accompanied me along the way.

With sincere appreciation,

[Ziainia mohamed El amine]

Summary

الملخص

أسهم التقدم في الإلكترونيات القوية وأنظمة التحكم الآلي في زيادة استخدام المحركات الحثية ضمن أنظمة القيادة الكهربائية. ويعود ذلك إلى متانتها، وكفاءتها العالية مقارنة بكتلتها، وانخفاض تكاليف تصنيعها. إن مراقبة هذه المحركات وصيانتها بشكل مبكر يساهم في زيادة فعالية التشغيل وتقليل الأعطال. يركز هذا العمل على نمذجة المحرك الحثي لمحاكاة حالات كسر قضبان الدوار، مع تطبيق تقنيات معالجة الإشارة المناسبة لاكتشاف الأعطال. وقد تم تطوير نموذج كامل وآخر مبسط للمحرك، تلاه تحليل طيفي لتيار الجزء الثابت للكشف الدقيق عن العيوب.

الكلمات المفتاحية: المحرك الحثي، كشف الأعطال، نمذجة انكسار القضبان، التحليل الطيفي.

Summary

Advancements in power electronics and automatic control systems have led to increased use of induction machines in electric drive systems. Their widespread adoption is attributed to their robustness, high power-to-weight ratio, and low production cost. To ensure optimal operation and reduce maintenance costs, early fault detection is essential. This thesis focuses on modeling induction machines to simulate rotor bar breakage and applying signal processing methods to detect faults effectively. A complete and reduced model of the machine is developed, followed by spectral analysis of stator current signals.

Keywords: Induction machine, Fault detection, Bar breakage modeling, Spectral analysis.

Résumé

Les progrès en électronique de puissance et en systèmes de commande automatique ont conduit à une utilisation accrue des machines asynchrones dans les systèmes d'entraînement électrique. Leur adoption généralisée est due à leur robustesse, leur rapport puissance/poids élevé et leur faible coût de production. Pour garantir un fonctionnement optimal et réduire les coûts de maintenance, une détection précoce des défauts est essentielle. Ce mémoire se concentre sur la modélisation des machines asynchrones pour simuler la rupture des barres du rotor et sur l'application de méthodes de traitement du signal pour détecter efficacement les défauts. Un modèle complet et réduit de la machine est développé, suivi d'une analyse spectrale des signaux de courant statorique.

Mots-clés : Machine asynchrone, Détection de défauts, Modélisation de la rupture de barre, Analyse spectrale.

Table of content

Summary i

Table of content ii

Notation and symbols vi

Acronyms and abbreviations viii

Table of figures ix

General introduction 1

Chapter I: Fault diagnosis of induction motors. 3

I.1 Introduction: 4

I.2 Induction motors: 4

I.2.1 Stator: 5

I.2.2 Rotor: 5

I.3 Working principle: 6

I.4 Types of induction motor faults: 6

I.4.1 Mechanical faults: 6

I.4.1.1 Bearing faults: 6

I.4.1.2 Eccentricity: 8

I.4.1.3 Unbalance: 9

I.4.1.3.1 Static unbalance: 9

I.4.1.3.2 Dynamic unbalance: 9

I.4.1.3.3 Couple unbalance: 10

I.4.1.3.4 Quasi-static unbalance: 10

I.4.2 Electrical faults: 11

I.4.2.1 Stator faults: 11

I.4.2.2 Rotor faults: 11

I.5 Methods of fault diagnosis: 12

I.5.1 Model-based methodologies: 12

I.5.2 Signal-based methodologies: 12
I.5.3 Data-driven methodologies: 12
I.5.4 Hybrid methodologies: 13
I.6 Conclusion: 13
Chapter II: Modeling of multi-winding system (magnetically coupled electric circuits method) 14
II.1 Introduction: 15
II.2 Calculation of inductances: 16
II.2.1 Stator: 16
II.2.2 Rotor: 17
II.2.3 Stator-rotor: 19
II.3 Establishing the equations: 20
II.3.1 Stator equations: 20
II.3.2 Rotor equations: 21
II.3.3 Mechanical equation: 25
II.4 Reduced size model: 26
II.5 Conclusion: 29
Chapter III: Simulation of multi-winding system 30
III.1 Introduction: 31
III.2 Simulation of the model: 31
III.3 Full model: 31
III.3.1 Healthy machine case no-load conditions: 32
III.3.2 Result interpretation: 34
III.3.3 Healthy machine case with load: 35
III.3.4 Result interpretation: 37
III.3.5 One broken case no-load condition: 38
III.3.6 Result interpretation: 40

III.3.7 One broken bar case with load: 41
III.3.8 Result interpretation: 43
III.3.9 Two adjacent broken bars with load: 44
III.3.10 Result interpretation: 46
III.4 Reduced model: 47
III.4.1 Healthy machine case no-load conditions: 48
III.4.2 Healthy machine case with load: 51
III.4.3 One broken bar: 53
III.4.4 Two adjacent broken bars: 54
III.5 Result interpretation (Comparison of the reduced model and the complete model): 55
III.5.1 No-load operation: 55
III.5.2 Operation under load: 56
III.5.3 Fault Representation 56
III.5.4 Oscillatory effects and harmonic interactions: 57
III.6 Conclusion: 57
Chapter IV: Spectral analysis of stator current 58
IV.1 Introduction: 59
IV.2 Spectral analysis approaches: 59
IV.2.1 Non-parametric methods: 59
IV.2.2 Parametric methods: 59
IV.3 Result of spectral analysis: 60
IV.3.1 Windowing in frequency domain analysis: 60
IV.3.2 Result of spectral analysis of stator current with 4 types of windowing, one broken bar case: 61
IV.3.3 Result of spectral analysis of stator current with Hanning Window, healthy machine case: 62
IV.3.4 Result of spectral analysis to study the effect of load: 63

IV.3.5 Result of spectral analysis to study the effect of position and number of broken bars: 64

IV.4 Conclusion: 65

General conclusion 67

Annex 70

Notation and symbols

Bs: Magnetic induction in the air gap created by the stator current [T]

C_{em}: Electromagnetic torque [N.m]

d, q: Indices for PARK transformation components, direct and quadrature, respectively

e: Air gap thickness [m]

f_s: Supply frequency [Hz]

g: Slip (%)

I_e: Short-circuit ring current [A]

I_{bk}: Bar current [A]

I_{rk}: rotor loop Current [A]

I_{ek}: Current in a portion of the ring [A]

I_{sabc}: Stator phase currents [A]

I_{ds}, I_{qs}: Two-phase components of the stator current, direct and quadrature [A]

J: Moment of inertia [Kg.m²]

K_f: Friction coefficient

L: Length of the magnetic circuit [m]

L_{sp}: Stator self-inductance [H]

L_{fs}: Stator leakage inductance [H]

L_b: Inductance of a rotor bar [H]

L_e: Short-circuit ring total inductance [H]

L_{rc}: Rotor cyclic inductance [H]

L_{sc}: Stator cyclic inductance [H]

M_{ss}: Mutual inductance between stator phases [H]

M_{rr}: Mutual inductance between rotor loops [H]

M_{sr}: Cyclic mutual inductance between the stator and rotor [H]

N_s: Number of stator turns per phase

N_r: Number of rotor bars

P: Power [W]

p: Number of pole pairs

R: Average radius of the air gap [m]

R_e: Short-circuit ring resistance [Ω]

R_r: Rotor bar resistance [Ω]

R_s: Stator winding resistance [Ω]

R_{bk}: Bar resistance [Ω]

R_{bc}: Defective bar resistance [Ω]

R_{bs}: Resistance of a healthy rotor bar [Ω]

R_{sp}: Resistance of a stator phase [Ω]

r,s: Indices for stator and rotor, respectively

θ: Angle describing a particular position in space, measured relative to a reference fixed to the stator [rad]

θ_r: Rotor position [rad]

θ_s: Position of stator quantities [rad]

Φ_{rk}: Magnetic flux created by a rotor loop [Wb]

Φ_s: Magnetic flux per pole created by the stator current [Wb]

Φ_{sabc}: Stator fluxes [Wb]

V_{sabc}: Stator voltages [V]

ω: Mechanical rotational speed [Rpm]

μ_0: Magnetic permeability of air [H/m]

Acronyms and abbreviations

AC: Alternative Current

AI: Artificial Intelligence

ANN: Artificial Neural Networks

AR: Autoregressive

FFT: Fast Fourier Transform

IIoT: Industrial Internet of Things

MCSA: Motor Current Signature Analysis

ML: Maximum Likelihood

MMF: Magnetomotive force

PCA: Principal Component Analysis

PSD: Power Spectral Density

RMF: Rotating Magnetic Field

SVM: Support Vector Machines

STFT: Short-Time Fourier Transform

Y-W: Yule-Walker

Table of figures

Figure I.1. Induction motor components. 4
Figure I.2. Stator lamination. 5
Figure I.3. Rotor cage. 5
Figure I.4. Dimensions and components of a bearing. 7
Figure I.5. Static and dynamic eccentricity. 8
Figure I.6. Static unbalance. 9
Figure I.7. Dynamic unbalance. 9
Figure I.8. Couple unbalance. 10
Figure I.9. Quasi-Static unbalance. 10
Figure I.10. Stator winding faults. 11
Figure I.11. Cracked bars and end ring. 12
Figure II.1. Structure of rotor cage. 17
Figure II.2. Magnetic induction produced by a single rotor loop. 18
Figure II.3. Equivalent representation of rotor loops. 21
Figure III.1. Simulink schematic of complete model. 31
Figure III.2. Electromagnetic torque and rotation speed in healthy machine case no-load conditions. 32
Figure III.3. Phase a current, I_{ds}/I_{qs} current and end ring current in healthy machine case no-load conditions. 33
Figure III.4. Current of ring portions 0 to 7, current of bar 0 to 7 and current of bar 0 in healthy machine case no-load conditions. 34
Figure III.5. Electromagnetic torque and rotation speed in healthy machine case with load. 35
Figure III.6. Phase a current, I_{ds}/I_{qs} current and end ring current in healthy machine case with load. 36
Figure III.7. Current of ring portions 0 to 7, current of bar 0 to 7 and current of bar 0 in healthy machine case with load. 37
Figure III.8. Electromagnetic torque and rotation speed in one broken bar case no-load condition. 38
Figure III.9. Phase a current, I_{ds}/I_{qs} current and end ring current in one broken bar case no-load condition. 39
Figure III.10. Current of ring portions 0 to 7, current of bar 0 to 7 and current of bar 0 in one broken bar case no-load condition. 40

Figure III.11. Electromagnetic torque and rotation speed in one broken bar case with load... 41
Figure III.12. Phase a current, I_{ds}/I_{qs} current and end ring current in one broken bar case with load. 42
Figure III.13. Current of ring portions 0 to 7, current of bar 0 to 7 and current of bar 0 in one broken bar case with load. 43
Figure III.14. Electromagnetic torque and rotation speed in two adjacent broken bars case with load. 44
Figure III.15. Phase a current, I_{ds}/I_{qs} current and end ring current in two adjacent broken bars case with load. 45
Figure III.16. Current of ring portions 0 to 7, current of bar 0 to 7 and current of bar 0 in two adjacent broken bars case with load. 46
Figure III.17. Simulink schematics of reduced model. 47
Figure III.18. Electromagnetic torque and rotation speed in healthy machine case no-load conditions. 48
Figure III.19. Phase a current, I_{ds}/I_{qs} and I_{dr}/I_{qr} currents in healthy machine case no-load conditions. 49
Figure III.20. Current of ring portions 0 to 7, current of bar 0 to 7 and current of bar 0 in healthy machine case no-load conditions..... 50
Figure III.21. Electromagnetic torque and rotation speed in healthy machine case with load. 51
Figure III.22. Phase a current, I_{ds}/I_{qs} and I_{dr}/I_{qr} currents in healthy machine case with load. .. 52
Figure III.23. Current of ring portions 0 to 7, current of bar 0 to 7 and current of bar 0 in healthy machine case with load. 53
Figure III.24. Electromagnetic torque and rotation speed in one broken bar case. 53
Figure III.25. Phase a current, I_{ds}/I_{qs} and I_{dr}/I_{qr} currents in one broken bar case. 54
Figure III.26. Electromagnetic torque and rotation speed in two adjacent broken bars case... 54
Figure III.27. Phase a current, I_{ds}/I_{qs} and I_{dr}/I_{qr} currents in two adjacent broken bars case..... 55
Figure IV.1. Result of spectral analysis of stator current with no windowing one broken bar case at t=1s. 60
Figure IV.2. Result of spectral analysis of stator current with Hamming, Hanning, Blackman and Kaiser windows. 61
Figure IV.3. Result of spectral analysis of stator current with Hanning Window, healthy machine case. 62
Figure IV.4. Result of spectral analysis of 2.3%, 4.3% and 7.2% for both healthy and one broken bar case. 63

Figure IV.5. Result of spectral analysis of adjacent and separate bar breaks in both two-bar and three-bar break cases. 64
Figure IV.6. Result of spectral analysis of evenly and non-evenly separate bar breaks. 65

General introduction

Induction motors, particularly squirrel cage motors, are the backbone of industrial applications due to their durability, efficiency, and low maintenance requirements. They are used extensively in industries such as manufacturing, energy, transportation, and automation, powering everything from conveyor belts and pumps to large-scale production machinery. Their simple design, absence of brushes, and ability to operate in harsh environments make them the preferred choice for many industrial systems.

Despite their reliability, induction motors are susceptible to various faults. Mechanical issues such as bearing failures and misalignment, stator faults including open circuits, phase-to-phase, coil-to-coil, turn-to-turn, and coil-to-ground short circuits, as well as rotor-related defects like broken bars and cracked end rings, can all impact motor performance. These faults can lead to efficiency losses, increased energy consumption, and unplanned downtime, resulting in significant economic losses for industries that depend on continuous operation.

The field of fault diagnosis in induction motors has evolved significantly, incorporating advanced techniques such as spectral analysis, artificial intelligence, and machine learning. Traditional methods, including Motor Current Signature Analysis (MCSA) and vibration analysis, have been widely used for identifying faults at an early stage. With the advent of smart monitoring systems and the Industrial Internet of Things (IIoT), real-time diagnostics and condition-based maintenance strategies are becoming increasingly prevalent in modern industrial setups which requires a solid model to base them on.

In this context, our work is mainly structured around four chapters:

The first chapter deals with the various faults that can occur in asynchronous machines, along with the different diagnostic methods used to detect them.

The second chapter focuses on the modeling of the asynchronous machine for simulating rotor bar breakage. It begins with the development of a multi-winding model using an analytical approach and proceeds to introduce a two-phase model through a generalized transformation.

The third chapter presents the simulation results obtained from the full and reduced-size model of the machine, in several operating conditions.

Finally, the fourth chapter is dedicated to fault analysis and processing, based on spectral analysis of the stator current using the Fast Fourier Transform (FFT).

Chapter I: Fault diagnosis of induction motors.

I.1 Introduction:

Due to their durability, induction motors are extensively used in applications demanding variable speeds and high power. However, they remain susceptible to various faults, and some may deteriorate prematurely, falling short of their expected lifespan. Detecting faults at an early stage is vital to reducing operational downtime and mitigating the risk of failures, especially in essential systems where motor performance is critical. A thorough understanding of the motor's characteristics, along with a well-structured mathematical model, is necessary to effectively diagnose mechanical and electrical faults [1] [2].

In this chapter, we present an overview of fault diagnosis in induction motors. We begin with the structure and working principles of induction motors, focusing on the stator and rotor. Common faults are then classified into mechanical and electrical types, including issues like bearing defects, unbalance, and rotor bar breakage.

We also outline the main diagnostic methods: model-based, signal-based, data-driven, and hybrid approaches. This chapter lays the foundation for the modeling and simulation of specific faults discussed in the following chapters.

I.2 Induction motors:

A squirrel cage induction motor consists of two main components:

- Stator: The stationary part of the motor that generates a rotating magnetic field.
- Rotor: The rotating part, shaped like a squirrel cage, which interacts with the stator's magnetic field to produce torque.

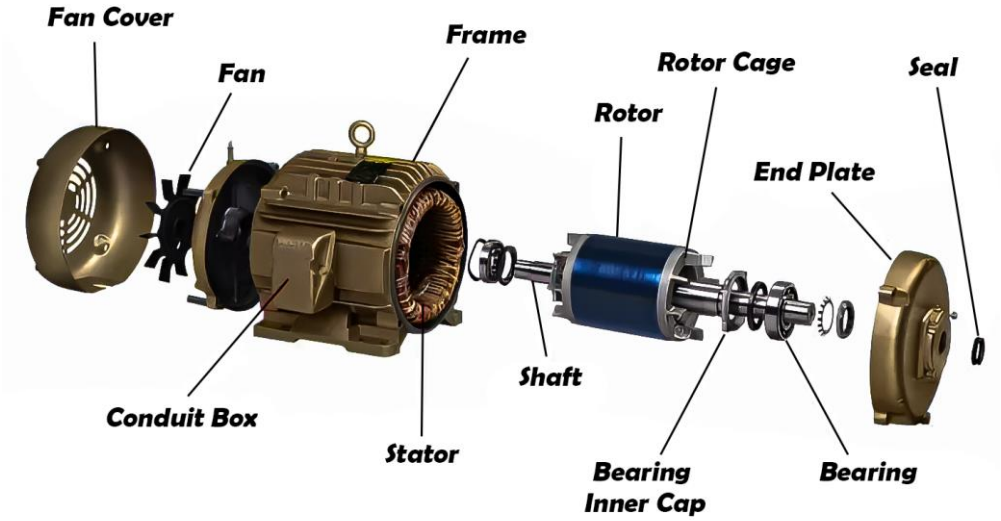


Figure I.1. Induction motor components [3].

I.2.1 Stator:

The stator is made of laminated iron cores to reduce eddy current losses and is fitted with three-phase windings. When a three-phase alternating current (AC) is supplied to the stator windings, it creates a rotating magnetic field (RMF). The speed of this RMF, called synchronous speed (Ns), is given by:

$$N_s = \frac{60 f_s}{p} \tag{1.1}$$

where:

f_s is the supply frequency (Hz),

p is the number of pole pairs.

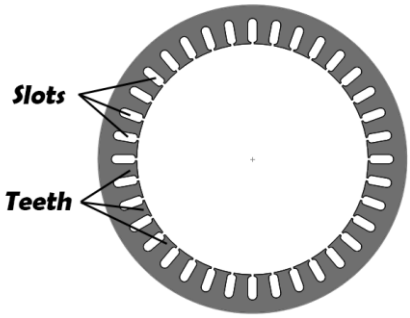


Figure I.2. Stator lamination.

I.2.2 Rotor:

The rotor consists of laminated iron cores with conductive bars (usually made of aluminum or copper) arranged in slots around the periphery. These bars are short-circuited at both ends by end rings, forming a closed-loop circuit. This structure is called the squirrel cage due to its resemblance to the exercise wheel of small rodents. Unlike wound rotors, squirrel cage rotors have no external electrical connections.

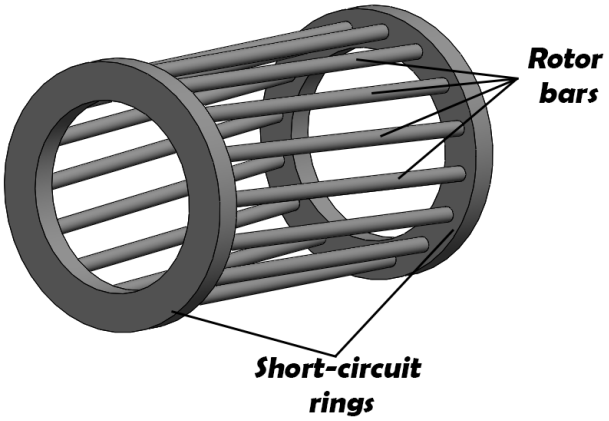


Figure I.3. Rotor cage.

I.3 Working principle:

The operation of a squirrel cage induction motor is based on Faraday's law of electromagnetic induction and Lenz's law:

- Generation of Rotating Magnetic Field: When a three-phase AC supply is fed to the stator, it generates a rotating magnetic field (RMF).
- Induced current in the rotor: The RMF cuts the rotor conductors, inducing an electromotive force (EMF) according to Faraday's law. Since the rotor is a closed circuit, the induced EMF causes current flow in the rotor bars.
- Production of Torque: The induced current in the rotor interacts with the stator's RMF, generating a force that drives the rotor in the same direction as the RMF. This is explained by Lenz's law, which states that the induced current opposes the cause that produces it.
- Slip and Rotor Speed: The rotor never reaches synchronous speed because if it did, no relative motion would exist between the stator field and rotor conductors, resulting in zero induced current and zero torque. The difference between synchronous speed (Ns) and rotor speed (Nr) is called slip (g), given by:

$$g = \frac{N_s - N_r}{N_s}.100\% \qquad (1.2)$$

I.4 Types of induction motor faults:

I.4.1 Mechanical faults:

I.4.1.1 Bearing faults:

Bearing faults can manifest in various forms, Raceway spalling occurs when the bearing's raceway surface deteriorates due to fatigue, leading to pitting and rough operation. Rolling element wear, such as ball or roller wear, results from continuous stress and insufficient lubrication, causing increased friction and reduced efficiency. Corrosion can develop due to exposure to moisture or contaminants, weakening the bearing structure over time. Cage deformation happens when the bearing's cage, which holds the rolling elements in place, becomes misshapen due to excessive load or overheating, leading to misalignment and irregular movement. Lubrication failures, whether due to contamination, insufficient lubrication, or degradation of lubricant properties, increase friction and accelerate wear. Misalignment occurs when the bearing is not properly positioned relative to the shaft, causing uneven load

distribution and excessive stress. Lastly, excessive clearance, or play, within the bearing can lead to instability, vibrations, and premature failure, further compromising machine reliability [4].

Each type of bearing fault is associated with a specific characteristic frequency, denoted as (f_c). This frequency corresponds to the periodic occurrence of anomalies caused by the fault. The characteristic frequencies depend on the bearing's geometric properties and the rotor's mechanical frequency (f_r). The mathematical expressions for these frequencies, corresponding to the three types of faults considered, are as follows [5].

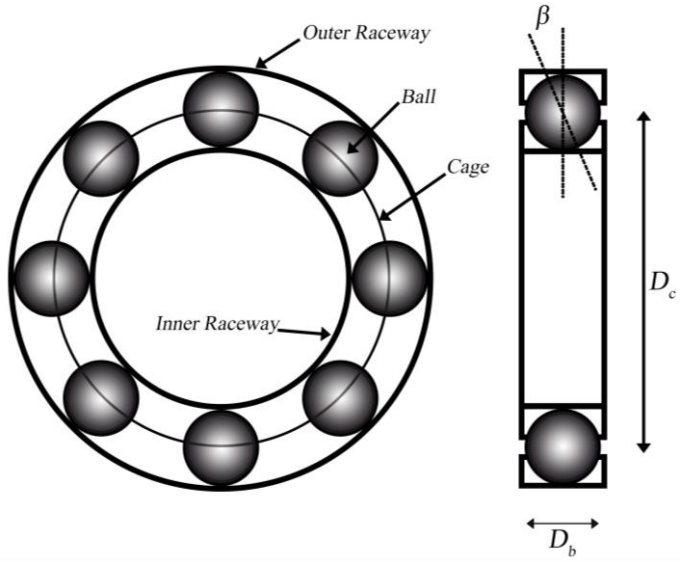


Figure I.4. Dimensions and components of a bearing.

Outer raceway deterioration

$$f_o = \frac{N_b}{2} . f_r \left(1 - \frac{D_b}{D_c} cos\beta\right) \quad (1.3)$$

Inner raceway deterioration

$$f_i = \frac{N_b}{2} . f_r \left(1 + \frac{D_b}{D_c} cos\beta\right) \quad (1.4)$$

Rolling element deterioration

$$f_b = \frac{D_b}{D_c} . f_r \left(1 - \frac{D_b}{D_c} cos\beta\right) \quad (1.5)$$

I.4.1.2 Eccentricity:

The variation in the air gap length leads to fluctuations in the density of the magnetic flux within the gap, which electrically affects the stator windings. These effects are observable in the current spectrum [6].

Three types of eccentricity can be distinguished:

- Static eccentricity: The rotor is displaced from the center of the stator bore but continues to rotate around its own axis.
- Dynamic eccentricity: The rotor remains centered within the bore but no longer rotates around its own axis.
- Mixed eccentricity: A combination of both static and dynamic eccentricities.

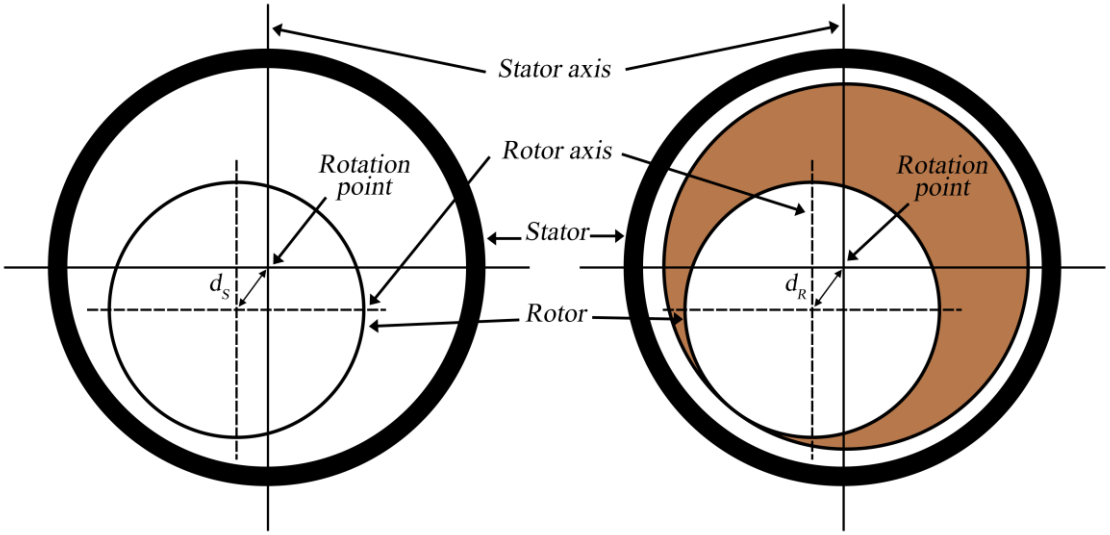


Figure I.5. Static and dynamic eccentricity.

In static eccentricity, d_s remain constant, whereas in dynamic eccentricity, d_R varies, causing the shaft to traverse the brown area depicted in Figure I.5.

The causes of eccentricity can include incorrect positioning of bearings during assembly, bearing wear, or shaft bending. Identifying the type of eccentricity can be done by analyzing specific frequency components in the phase current spectrum [6].

For static eccentricity, characteristic frequency components can be expressed as:

$$f_{ecc} = f_s \left(1 \mp \frac{n\, N_r (1-g)}{p}\right) \tag{1.6}$$

For dynamic eccentricity:

$$f_{ecc} = f_s \left(1 \mp 2n(1-g)\right) \tag{1.7}$$

For misalignment:

$$f_{ecc} = f_s \left(1 \mp \frac{n(1-g)}{p}\right) \quad (1.8)$$

These components allow for the identification and classification of eccentricity types based on spectral analysis.

I.4.1.3 Unbalance:

I.4.1.3.1 Static unbalance:

Static unbalance occurs when the rotor's center of rotation is offset from its geometric center but remains parallel to it. As a result, when the rotor is stationary, the heavier side naturally settles at the lowest point [7].

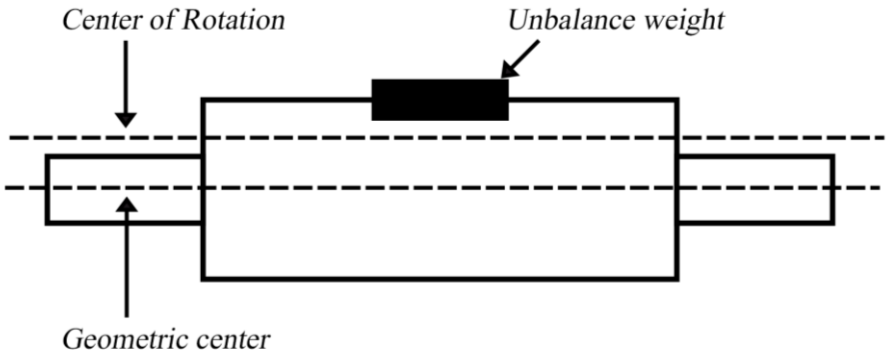


Figure I.6. Static unbalance.

I.4.1.3.2 Dynamic unbalance:

Dynamic unbalance occurs when the rotor's center of rotation does not align with its geometric centerline. Unlike static unbalance, the center of rotation is not necessarily parallel to the rotor's geometric center, meaning there is no single heavy side that settles at rest. This type of unbalance only becomes apparent when the rotor is spinning, generating vibrations [7].

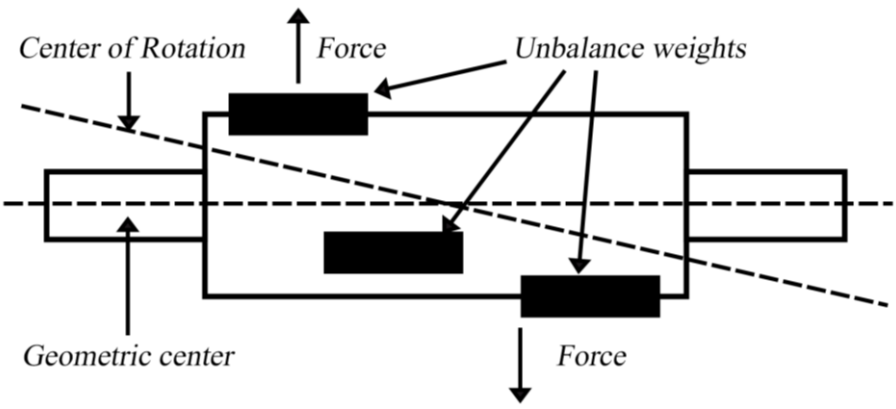


Figure I.7. Dynamic unbalance.

I.4.1.3.3 Couple unbalance:

Couple unbalance occurs when the rotor's mass is unevenly distributed in such a way that two equal but opposite forces act on different planes. Unlike static and dynamic unbalance, this results in a tilting effect rather than a simple shift in mass. Since there is no single heavy side, the unbalance only becomes noticeable when the rotor is spinning [7].

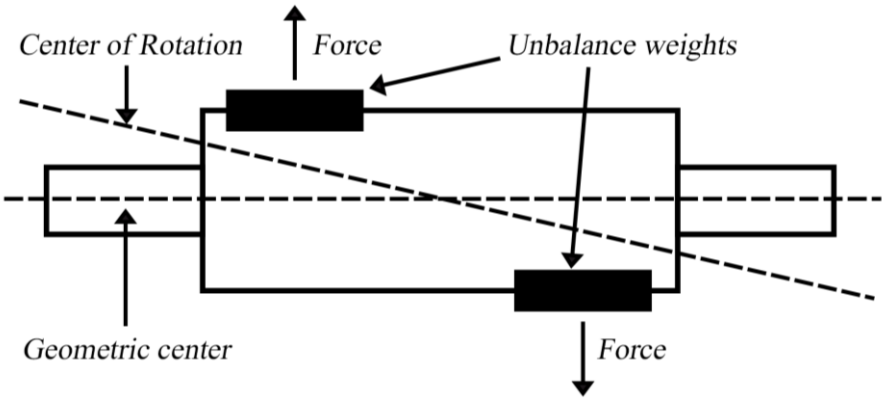


Figure I.8. Couple unbalance.

I.4.1.3.4 Quasi-static unbalance:

Quasi-static unbalance occurs when the rotor's center of rotation crosses its geometric centerline but does not align with its center of gravity. This means the mass is unevenly distributed along the axis, causing both static and dynamic effects [7].

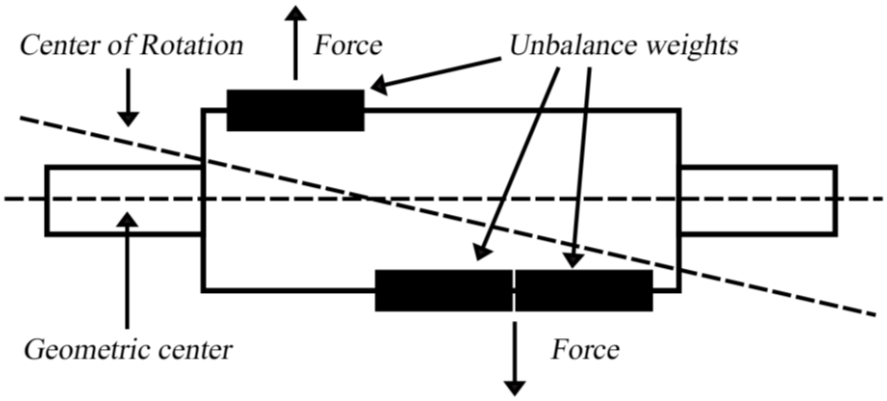


Figure I.9. Quasi-Static unbalance.

I.4.2 Electrical faults:

I.4.2.1 Stator faults:

Stator faults primarily manifest as short circuits, which typically occur in four forms:

- Phase-to-phase short circuit: where a fault develops between two different phases
- Coil-to-coil short circuit: occurring between two coils within the same phase
- Turn-to-turn short circuit: where a short forms between individual turns of the same winding
- Coil-to-ground short circuit: where a coil is shorted to the ground.

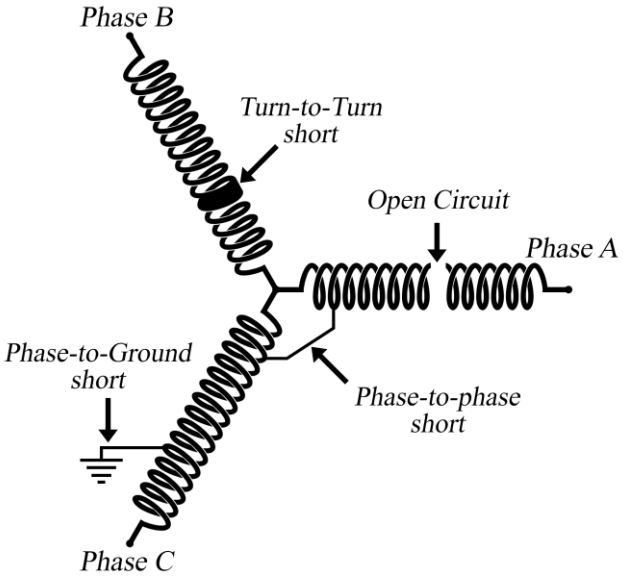


Figure I.10. Stator winding faults.

Studies have shown that the stator phase current exhibits a spectrum enriched with harmonics due to the short circuit between one or more stator turn, the mathematical expressions for these frequencies is as follows:

$$f_{short} = f_s.\left(\frac{n(1-g)}{p} \mp k\right) \tag{1.9}$$

I.4.2.2 Rotor faults:

Rotor faults primarily manifest as cracked end rings and broken bars, which are difficult to detect since the machine continues to function despite their presence. When a bar or ring breaks, the current redistributes to the remaining bars, increasing their load and making them more prone to failure. This process continues progressively until a critical number of bars and rings are damaged, ultimately leading to machine shutdown.

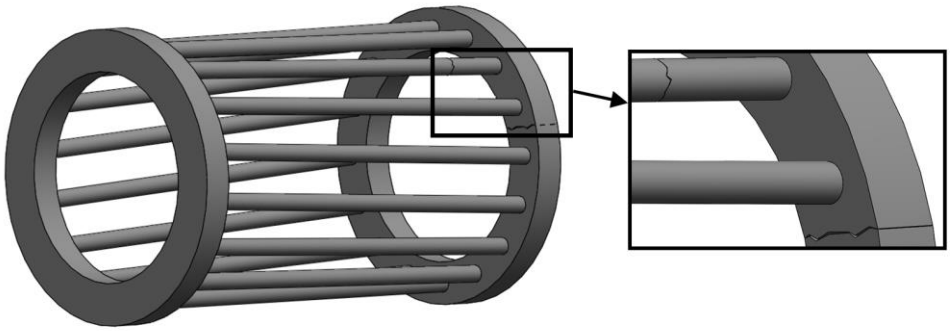


Figure I.11. Cracked bars and end ring.

I.5 Methods of fault diagnosis:

I.5.1 Model-based methodologies:

Model-based methodologies rely on mathematical models to represent the behavior of a system under normal and faulty conditions. These approaches leverage analytical redundancy rather than hardware redundancy, meaning that faults are detected through discrepancies between the predicted and observed system responses. Techniques such as observer-based fault diagnosis, parity space methods, and parameter estimation are commonly employed [1]. A primary advantage of model-based methods is their robustness in diagnosing faults with minimal reliance on historical data. However, their effectiveness depends on the accuracy of the mathematical model, making them less suitable for complex systems with high variability or unmodeled dynamics.

I.5.2 Signal-based methodologies:

Signal-based methodologies focus on analyzing measured signals rather than relying on explicit mathematical models. These methods assume that faults introduce distinguishable changes in system signals, which can be captured using time-domain, frequency-domain, or time-frequency-domain analysis. Common techniques include Fast Fourier Transform (FFT), wavelet transforms, and statistical feature extraction. These approaches are widely used in real-time applications such as monitoring mechanical components and electrical systems. While signal-based methods are effective in detecting abnormalities, their diagnostic accuracy may suffer when dealing with noisy environments or complex fault interactions.

I.5.3 Data-driven methodologies:

Data-driven methodologies exploit large volumes of historical data to identify and diagnose faults. Unlike model-based methods, which require explicit system modeling, data-driven approaches infer patterns from data using machine learning, statistical analysis, and artificial

intelligence techniques such as Principal Component Analysis (PCA), Support Vector Machines (SVM), and Artificial Neural Networks (ANN). These methods are particularly useful in industrial settings where system models are difficult to obtain. However, they require significant computational resources and high-quality training data to achieve reliable fault detection and classification.

I.5.4 Hybrid methodologies:

Hybrid methodologies integrate multiple diagnostic approaches to leverage their respective strengths while mitigating their weaknesses. For example, combining model-based and signal-based methods can improve fault detection robustness, while integrating data-driven techniques can enhance diagnostic accuracy. Recent research has explored hybrid systems incorporating statistical feature extraction with machine learning classifiers for complex applications such as rotating machinery fault detection and chemical process monitoring. The main challenge in hybrid methodologies lies in their implementation complexity, requiring careful tuning of individual components to achieve optimal performance [8] [1].

I.6 Conclusion:

In this chapter, we provided a comprehensive overview of fault diagnosis in induction motors, emphasizing their critical role in industrial applications. We began with an introduction to induction motors, detailing their primary components, including the stator and rotor, and their fundamental working principles. Understanding these elements is essential for diagnosing and preventing faults that may compromise motor performance.

We then categorized the common faults affecting induction motors into mechanical and electrical types. Mechanical faults, such as bearing defects, eccentricity, and various forms of unbalance (static, dynamic, couple, and quasi-static), were discussed in detail, highlighting their causes and potential consequences. Similarly, electrical faults, including stator and rotor-related issues, were analyzed to illustrate their impact on motor efficiency and reliability.

Furthermore, we explored various fault diagnosis methodologies, classified into model-based, signal-based, data-driven, and hybrid approaches. Each of these techniques offers distinct advantages depending on the application, accuracy requirements, and available data. Model-based methods rely on mathematical representations of motor behavior, signal-based methods analyze electrical and mechanical signals, data-driven methods leverage machine learning and statistical analysis, and hybrid approaches integrate multiple techniques for improved accuracy. The analysis and interpretation of these diagnostic methods require prior knowledge of a good machine model, which will be the subject of the second chapter.

Chapter II: Modeling of multi-winding system (magnetically coupled electric circuits method)

II.1 Introduction:

The analysis of induction machines can be approached using three primary methods: electromagnetic field theory, governed by Maxwell's equations; electrical circuit theory, based on Kirchhoff's laws; or a hybrid methodology integrating both frameworks [1]. Two fundamental modeling approaches are commonly employed:

- Local approach: This method focuses on the characterization of local quantities, such as magnetic flux density, and typically employs numerical techniques like finite element analysis. It is particularly useful for examining localized physical phenomena, including faults in the machine's rotor cage.
- Analytical approach: This method analyzes global external parameters, such as current and electromagnetic torque, utilizing an equivalent electrical circuit model of the machine derived from Kirchhoff's laws. Additionally, it incorporates the "two-axis transformation" to simplify the electrical equations governing multi-winding systems. Given its efficiency and analytical tractability, this approach has been selected as the methodological foundation for this study.

multi-winding system (magnetically coupled electric circuits method):

This approach interprets the machine from the perspective of circuit theory. To facilitate simulation and troubleshoot issues related to rotor bar and end ring breakages, the rotor has been modeled using interconnected electrical loops that are magnetically coupled.

To streamline the modeling process, the following simplifying assumptions are made:

- The air gap is considered constant, and the effects of slotting are neglected.
- The relative permeability of the iron core is assumed to be infinitely large.
- The distribution of the magnetomotive force (MMF) and the magnetic flux in the air gap follows a sinusoidal pattern.
- Saturation effects, skin effects, and eddy currents (except within the rotor bars) are disregarded.
- Additionally, it is assumed that the stator is in ideal condition, exhibiting symmetrical construction.

II.2 Calculation of inductances:

II.2.1 Stator:

It is assumed that the stator windings are ideally distributed around the air gap peripheral so that the resulting induction can be sinusoidal, in this case The magnetomotive force (MMF) will be:

$$F(\theta) = \frac{2\,N_s\,I_s}{\pi\,p}\,cos(\theta) \tag{2.1}$$

According to Ampere's theorem:

$$F(\theta) = \oint H\,dl\; = \frac{N_s\,I_s}{p} \tag{2.2}$$

The maximum induction in the air gap can be obtained using equation (2.2):

$$B_{max} = \mu_0\,\frac{N_s\,I_s}{2\,p\,e} \tag{2.3}$$

The induction decomposition becomes:

$$B(\theta) = 2\,\mu_0\,\frac{N_s\,I_s}{e\,\pi\,p}\,cos(p\theta) \tag{2.4}$$

The magnetic flux in the air gap can be obtained by integrating equation (2.4):

$$\phi_s = \iint_s B_s\,ds = \int_0^t dz \int_{-\frac{1}{2}}^{\frac{1}{2}} B_s\,R\,l\,d\theta \tag{2.5}$$

Solving for flux:

$$\phi_s = \frac{4}{\pi}\,\mu_0\,l\;R\,\frac{N_s\,I_s}{e\,p^2} \tag{2.6}$$

The total flux crossing the winding of phase "a":

$$\phi_{sa} = N_s\,\phi_s = N_s^2\,I_s\,\frac{2\,\mu_0\,R\,L}{e\,p\,\pi}\int_{-\frac{1}{2}}^{\frac{1}{2}}\cos(p\theta)\;d\theta \tag{2.7}$$

Thus:

$$\phi_{sa} = L_{sp}\,I_s \tag{2.8}$$

The main inductance of the stator phase "a" using equation (2.7):

$$L_{sp} = 4\,\mu_0\; L\, R \frac{N_s^2}{e\, p^2\, \pi} \tag{2.9}$$

The leakage flux:

$$\phi_{fs} = L_{fs}\, I_s \tag{2.10}$$

The total inductance of phase "a":

$$L_{as} = L_{sp} + L_{fs} \tag{2.11}$$

Since the stator windings are symmetrical, the self-inductances of the three phases are:

$$L_{as} = L_{bs} = L_{cs} = L_s \tag{2.12}$$

II.2.2 Rotor:

The cage rotor is represented by Figure II.1, it shows the circuit representing the end rings and bars of the rotor, which allows us to consider any type of breakage, whether it's in the ring or in bars.

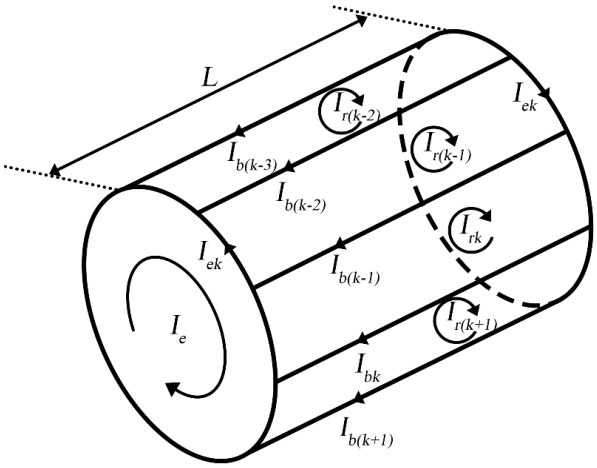


Figure II.1. Structure of rotor cage.

I_{rk} Represents the loop current k and I_{bk} the bar current k, with:

$$I_{bk} = I_{rk} - I_{r(k+1)} \tag{2.13}$$

Figure II.2 represents the shape of the supposed radial magnetic induction produced by a rotor loop in the air gap.

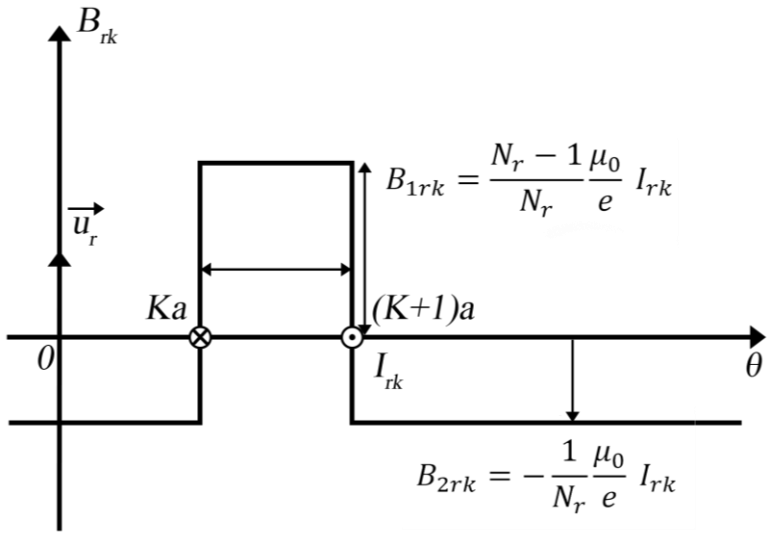


Figure II.2. Magnetic induction produced by a single rotor loop.

The spatial distribution of the field generated by the rotor current loop is assumed to be rectangular. The main inductance and the mutual inductance of a rotor mesh are determined based on the expression of the self-flux of loop k. Thus, we have:

Flux linkage of rotor loop k:

$$\phi_{rpk} = \int_0^t dz \int_{ka}^{(k+1)a} B_{1rk}\, R\, L\, d(\theta) \tag{2.14}$$

Expression for the flux:

$$\phi_{rpk} = \frac{N_r - 1}{N_r^2} \times \frac{2\,\mu_0\,\pi\,L\,R}{e}\, I_{rk} \tag{2.15}$$

Self-inductance of a rotor loop:

$$L_{rp} = \frac{N_r - 1}{Nr^2} \times \frac{2\,\mu_0\,\pi\,L\,R}{e} \tag{2.16}$$

Total inductance of rotor loop k:

$$L_{rr} = L_{rp} + 2L_b + 2\,L_e \tag{2.17}$$

Rotor loops are magnetically coupled with the gap flux, the flux traveling the j loop produced by the current I_{rk} that circulates the loop k is given by:

$$\phi_{rjrk} = \int_0^t dz \int_{ja}^{(j+1)a} B_{2rk}\, R\, L\, d(\theta) \tag{2.18}$$

$$\phi_{rjrk} = \int_0^t dz \int_{ja}^{(j+1)a} \left(-\frac{\mu_0\, L\, R}{e\, N_r}\, I_{rk}\right) d(\theta) \tag{2.19}$$

From the equation (2.19) we obtain the Mutual inductance between rotor loops:

$$M_{rr} = -\frac{\mu_0\, 2\, \pi\, L\, R}{e\, N_r^2} \tag{2.20}$$

II.2.3 Stator-rotor:

Mutual inductance between stator phase n and rotor loop k with n= (1,2,3) is given by:

$$B_{msr} = \frac{2\, \mu_0\, N_s\, I_s}{e\, p\, \pi}\, cos\left(p\theta - n\, \frac{\pi}{3}\right) \tag{2.21}$$

$$\phi_{rpk} = \int_0^t dz \int_{ka}^{(k+1)a} B_{msr}\, R\, L\, d(\theta) \tag{2.22}$$

We get:

$$\phi_{rka} = -\frac{2\, \mu_0\, N_s\, I_s}{e\, p\, \pi}\, \frac{L.R}{p}\, \left[sin\left(p\theta - n\, \frac{\pi}{3}\right)\right]_{ka}^{(k+1)a} \tag{2.23}$$

Mutual inductance expression between phase "a" and the rotor loop k is given by:

$$M_{rka} = -M_{sr}\, cos\left(p\theta - n\, \frac{2.\pi}{3} + ka\right) \tag{2.24}$$

With

$$M_{sr} = \frac{4\, \mu_0\, N_s\, R\, L}{e\, p^2\, \pi}\, \sin\left(\frac{a}{2}\right) \tag{2.25}$$

And

$$a = p\frac{2.\pi}{N_r} \tag{2.26}$$

Representing the electrical angle between two rotor loops.

II.3 Establishing the equations:

II.3.1 Stator equations:

Stator voltage and flux equations:

$$[V_{sabc}] = [R_s][I_{sabc}] + \frac{d}{dt}[\phi_{sabc}] \quad (2.27)$$

$$[\phi_{sabc}] = [L_s][I_{sabc}] + [M_{sr}][I_{rk}] \quad (2.28)$$

With

$$[V_{sabc}] = [V_{sa} \quad V_{sb} \quad V_{sc}]^t \quad (2.29)$$

$$[I_{sabc}] = [I_{sa} \quad I_{sb} \quad I_{sc}]^t \quad (2.30)$$

$$[\phi_{sabc}] = [\phi_{sa} \quad \phi_{sb} \quad \phi_{sc}]^t \quad (2.31)$$

$$[I_{rk}] = \left[I_{r0} \quad I_{r1} \quad \dots \quad I_{r(Nr-1)}\right]^t \quad (2.32)$$

Stator resistance matrix:

$$[R_s] = \begin{bmatrix} R_{sp} & 0 & 0 \\ 0 & R_{sp} & 0 \\ 0 & 0 & R_{sp} \end{bmatrix} \quad (2.33)$$

Stator inductance matrix:

$$[L_s] = \begin{bmatrix} L_{sp} + L_{fs} & M_{ss} & M_{ss} \\ M_{ss} & L_{sp} + L_{fs} & M_{ss} \\ M_{ss} & M_{ss} & L_{sp} + L_{fs} \end{bmatrix} \quad (2.34)$$

Mutual inductance between stator and rotor with (k=1,2,3 …….,Nr-1):

$$[M_{sr}] = \begin{bmatrix} \dots & \dots & -M_{sr}\cos(\theta_r + ka) & \dots & \dots \\ \dots & \dots & -M_{sr}\cos\left(\theta_r + ka - \frac{2\pi}{3}\right) & \dots & \dots \\ \dots & \dots & -M_{sr}\cos\left(\theta_r + ka + \frac{2\pi}{3}\right) & \dots & \dots \end{bmatrix} \quad (2.35)$$

II.3.2 Rotor equations:

Figure II.3 presents a k-loop of the rotor, and shows the conventions chosen for the currents.

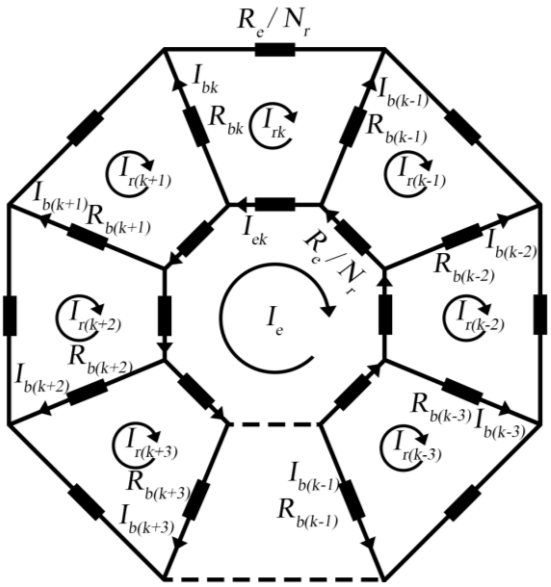


Figure II.3. Equivalent representation of rotor loops.

Knowing that:

$$I_{ek} = I_{rk} - I_e \tag{2.36}$$

$$I_{bk} = I_{rk} - I_{r(k-1)} \tag{2.37}$$

Electrical equation for rotor loop k:

$$\frac{R_e}{N_r} I_{rk} - R_{b(k-1)} I_{b(k-1)} + \frac{R_e}{N_r} I_{ek} + \frac{d}{dt}\phi_{rk} = 0 \tag{2.38}$$

The total flux Φ_{rk} for rotor loop k is the sum of terms below:

$$\phi_{rk} = \phi_{rp} + \phi_{rr} + \phi_{sr} \tag{2.39}$$

With Φ_{rp} representing the main flux:

$$\phi_{rp} = L_{rp} I_{rk} \tag{2.40}$$

And Φ_{rr} representing the Mutual flux with the other loops of the rotor:

$$\phi_{rr} = M_{rr} \sum_{\substack{j=0 \\ j\neq k}}^{N_r-1} I_{rj} \tag{2.41}$$

Φ_{sr} represents the Mutual flux with the stator:

$$\phi_{sr} = M_{sr} \left[cos\,(\theta_r + ka) : cos\left(\theta_r + ka - \frac{2\pi}{3}\right) : cos\left(\theta_r + ka - \frac{4\pi}{3}\right)\right][I_{abc}] \tag{2.42}$$

Equation (2.38) becomes:

$$R_{bk}\, I_{r(k-1)} + \left(2\frac{R_e}{N_r} + R_{b(k-1)} + R_{bk}\right) I_{rk} - R_{bk}\, I_{r(k+1)} - \frac{R_e}{N_r}\, I_e + \frac{d}{dt}\phi_{rk} = 0 \tag{2.43}$$

Then the total sum becomes

$$\phi_{rk} = \left(L_{rp} + \frac{2.L_e}{N_r} + 2L_b\right) I_{rk} - L_b\left(I_{r(k-1)} + I_{r(k+1)}\right) - \frac{L_e}{N_r}\, I_e - M_{rr} \sum_{\substack{j=0 \\ j\neq k}}^{N_r-1} I_{rj}$$
$$- M_{sr} \left[cos\,(\theta_r + ka) : cos\left(\theta_r + ka - \frac{2\pi}{3}\right) : cos\left(\theta_r + ka - \frac{4\pi}{3}\right)\right][I_{abc}] \tag{2.44}$$

with (k=1,2,3 …….,Nr-1)

A factor of 3/2 is applied compared to the stator equation due to the Clarke transformation.

The terms L_b and L_e represent rotor leakage inductances.

$$\phi_{rk} = \left(L_{rp} + \frac{2.L_e}{N_r} + 2L_b\right) I_{rk} - L_b\left(I_{r(k-1)} + I_{r(k+1)}\right) - \frac{L_e}{N_r}\, I_e - M_{rr} \sum_{\substack{j=0 \\ j\neq k}}^{N_r-1} I_{rj}$$
$$- \frac{3}{2} M_{sr}\left(I_{ds}\cos(ka) + I_{qs}\sin(ka)\right) \tag{2.45}$$

We calculate the derivative:

$$\frac{d\phi_{rk}}{dt} = \left(L_{rp} + \frac{2.L_e}{N_r} + 2L_b\right)\frac{dI_{rk}}{dt} - L_b\left(\frac{dI_{r(k-1)}}{dt} + \frac{dI_{r(k+1)}}{dt}\right) - \frac{L_e}{N_r}.\frac{dI_e}{dt} - M_{rr} \sum_{\substack{j=0 \\ j\neq k}}^{N_r-1} \frac{dI_{rj}}{dt}$$
$$- \frac{3}{2} M_{sr}\left(\frac{dI_{ds}}{dt}\cos(ka) + \frac{dI_{qs}}{dt}\sin(ka)\right) \tag{2.46}$$

The flux induced in the rotor loop is given by:

$$\phi_{rk} = L_{rp}\, I_{rk} - L_b \left(I_{b(k-1)} - I_{bk}\right) - \frac{L_e}{N_r}(I_{ek} + I_{ek}) + M_{rr} \sum_{\substack{j=0 \\ j\neq k}}^{N_r-1} I_{rj} - \frac{3}{2} M_{sr}\, (I_{ds}\cos(ka) + I_{qs}\sin(ka)) \tag{2.47}$$

We replace equation (2.46) in equation (2.38) we get:

$$\left(L_{rp} + \frac{2L_e}{N_r} + 2L_b\right)\frac{dI_{rk}}{dt} \pm M_{rr} \sum_{\substack{j=0 \\ j\neq k}}^{N_r-1} \frac{dI_{rj}}{dt} - L_b\left(\frac{dI_{r(k-1)}}{dt} + \frac{dI_{r(k+1)}}{dt}\right) - \frac{3}{2} M_{sr}\left(\frac{dI_{ds}}{dt}\cos(ka) + \frac{dI_{qs}}{dt}\sin(ka)\right) - \frac{L_e}{N_r}\frac{dI_e}{dt} = R_{bk}\, I_{r(k-1)} + \left(2\frac{R_e}{N_r} + R_{b(k-1)} + R_{bk}\right) I_{rk} - R_{bk}\, I_{r(k+1)-} \frac{R_e}{N_r}\, I_e \tag{2.48}$$

Equation for the short-circuit ring:

$$\frac{L_e}{N_r} \sum_{k=0}^{N_r-1} \frac{dI_{rk}}{dt} - L_e\, \frac{dI_e}{dt} - \left(R_e\, I_e - \frac{R_e}{N_r} \sum_{k=0}^{N_r-1} I_{rk}\right) = 0 \tag{2.49}$$

With the same method, we use I_{ek} and I_{bk} we find:

$$\frac{R_e}{N_r} \sum_{k=1}^{N_r} I_{rk} + \frac{L_e}{N_r} \sum_{k=1}^{N_r} \frac{dI_{rk}}{dt} - L_e\, \frac{dI_e}{dt} - R_e\, I_e = 0 \tag{2.50}$$

State-space representation of the system:

$$[L]\frac{d[I]}{dt} = [V] - [R][I] \tag{2.51}$$

The global system becomes:

$$
\begin{bmatrix}
L_{sc} & 0 & \cdots & \cdots & -M_{sr}cosja & \cdots & 0 \\
0 & L_{sc} & \cdots & \cdots & -M_{sr}sinja & \cdots & 0 \\
\vdots & \vdots & L_{rp}+\frac{2.L_e}{N_r}+2L_b & M_{rr}-L_b & M_{rr} & M_{rr} & M_{rr}-L_b \\
\vdots & \vdots & M_{rr}-L_b & L_{rp}+\frac{2.L_e}{N_r}+2L_b & M_{rr}-L_b & M_{rr} & M_{rr} \\
\vdots & \vdots & \cdots & \cdots & \cdots & \cdots & \cdots \\
-\frac{3}{2}M_{sr}coska & -\frac{3}{2}M_{sr}sinka & \cdots & \cdots & \cdots & \cdots & \cdots \\
\vdots & \vdots & M_{rr}-L_b & M_{rr} & M_{rr}-L_b & L_{rp}+\frac{2.L_e}{N_r}+2L_b & -\frac{L_e}{N_r} \\
0 & 0 & -\frac{L_e}{N_r} & \cdots & \cdots & -\frac{L_e}{N_r} & L_e
\end{bmatrix}
\begin{bmatrix}
\frac{d}{dt}\begin{bmatrix} I_{ds} \\ I_{qs} \\ I_{r0} \\ \vdots \\ I_{rj} \\ \vdots \\ I_{r(Nr-1)} \\ I_e \end{bmatrix}
\end{bmatrix}
+
\begin{bmatrix}
R_e & -wL_{sc} & \cdots & \cdots & M_{sr}wsinja & \cdots & 0 \\
-wL_{sc} & R_e & \cdots & \cdots & -M_{sr}wcosja & \cdots & 0 \\
0 & 0 & 2\frac{R_e}{N_r}+R_{b0}+R_{b(Nr-1)} & -R_{b0} & 0 & 0 & -R_{b(Nr-1)} \\
0 & 0 & 0 & -R_{b(Nr-1)} & 2\frac{R_e}{N_r}+R_{b0}+R_{b(Nr-1)} & -R_{bk} & 0 \\
0 & 0 & 0 & \cdots & \cdots & \cdots & \cdots \\
0 & 0 & 0 & \cdots & \cdots & \cdots & \cdots \\
0 & 0 & -R_{b(Nr-1)} & \cdots & -R_{b(Nr-2)} & 2\frac{R_e}{N_r}++R_{b(Nr-2)}+R_{b(Nr-1)} & -\frac{R_e}{N_r} \\
0 & 0 & -\frac{R_e}{N_r} & \cdots & \cdots & -\frac{R_e}{N_r} & R_e
\end{bmatrix}
\begin{bmatrix} I_{ds} \\ I_{qs} \\ I_{r0} \\ \vdots \\ I_{rj} \\ \vdots \\ I_{r(Nr-1)} \\ I_e \end{bmatrix}
-
\begin{bmatrix} V_{ds} \\ V_{qs} \\ 0 \\ 0 \\ 0 \\ 0 \\ 0 \\ 0 \end{bmatrix}
=
\begin{bmatrix} 0 \\ 0 \\ -\frac{R_e}{N_r} \\ \vdots \\ \vdots \\ \vdots \\ -\frac{R_e}{N_r} \\ R_e \end{bmatrix}
\tag{2.52}
$$

II.3.3 Mechanical equation:

The instantaneous power absorbed by the asynchronous machine is given by the expression:

$$P_e = V_a I_a + V_b I_b + V_c I_c = [V_{sabc}]^t [I_{sabc}]^t \quad (2.53)$$

We apply Park transformation to get:

$$P_e = V_{ds} I_{ds} + V_{qs} I_{qs} \quad (2.54)$$

Knowing that:

$$V_{ds} = R_s I_{ds} + \frac{d\phi_{ds}}{dt} - w\phi_{qs} \quad (2.55)$$

$$V_{qs} = R_s I_{qs} + \frac{d\phi_{qs}}{dt} + w\phi_{qs} \quad (2.56)$$

We replace the voltages with the expressions of V_{ds} and V_{qs}:

$$P_e = R_s \left({I_{ds}}^2 + {I_{qs}}^2\right) + \frac{d\phi_{ds}}{dt} I_{qs} + \frac{d\phi_{qs}}{dt} I_{ds} + w\left(\phi_{qs} I_{qs} - \phi_{qs} I_{ds}\right) \quad (2.57)$$

with $w(\phi_{qs}.I_{qs} - \phi_{qs}.I_{ds})$ representing the electromagnetic power.

we have:

$$P_e = \frac{w}{p} C_e \quad (2.58)$$

$$C_{em} = p\left[\phi_{ds} I_{qr} - \phi_{qs} I_{dr}\right] \quad (2.59)$$

We get:

$$C_{em} = pM\left[I_{ds} I_{qr} - I_{qs} I_{dr}\right] \quad (2.60)$$

The electromagnetic torque is obtained by co-energy derivation:

$$C_{em} = \frac{3}{2} p \left[I_{sdq}\right]^t \frac{d}{d\theta} \begin{bmatrix} \cdots & -M_{sr} \cos(\theta_r + ka) & \cdots \\ \cdots & -M_{sr} \cos(\theta_r + ka) & \cdots \end{bmatrix} \begin{bmatrix} \vdots \\ I_{rk} \\ \vdots \end{bmatrix} \quad (2.61)$$

$$C_{em} = \frac{3}{2} p M_{sr} \left\{ I_{ds} \sum_{k=0}^{N_r - 1} I_{rk} \sin ka - I_{qs} \sum_{k=0}^{N_r - 1} I_{rk} \cos ka \right\} \quad (2.62)$$

We add the mechanical equations to obtain the speed:

$$\frac{d\Omega}{dt} = \frac{1}{J}\, P\left(C_e - C_r - \frac{kf}{p}w\right) \tag{2.63}$$

$$\frac{d\theta r}{dt} = w \tag{2.64}$$

II.4 Reduced size model:

The system representation given by equation reveals a high-order system, as it comprises the number of stator phases, rotor loops, and electromechanical equations.

To simplify the analysis, we applied an extended Park transformation to the rotor system, converting the multi-windings representation into a two-axis (d,q) system.

The power invariant park transformation matrix with an a-phase to d-axis alignment is given by:

$$\begin{bmatrix} \mathrm{d} \\ q \\ 0 \end{bmatrix} = \sqrt{\frac{2}{3}} \begin{bmatrix} \cos(\theta) & \cos\left(\theta - \frac{2\pi}{3}\right) & \cos\left(\theta + \frac{2\pi}{3}\right) \\ \sin(\theta) & \sin\left(\theta - \frac{2\pi}{3}\right) & \sin\left(\theta + \frac{2\pi}{3}\right) \\ \sqrt{\frac{1}{2}} & \sqrt{\frac{1}{2}} & \sqrt{\frac{1}{2}} \end{bmatrix} \begin{bmatrix} \mathrm{a} \\ b \\ c \end{bmatrix} \tag{2.65}$$

We can define a state vector [X], which, after applying the transformation matrix:

$$\left[X_{sdq0}\right] = [T(\theta_s)][X_{sabc}] \rightarrow [X_{sabc}] = [T(\theta_s)]^{-1}\left[X_{sdq0}\right] \tag{2.66}$$

$$\left[X_{rdq0}\right] = [T_{3Nr}(\theta_r)][X_{rk}] \rightarrow [X_{sabc}] = \left[T_{3Nr}\left(\theta_{ref}\right)\right]^{-1}\left[X_{rdq0}\right] \tag{2.67}$$

Stator part:

$$[V_s] = [R_s][I_s] + \frac{d\{[I_s][L_s]\}}{dt} + \frac{d\{[I_{rk}][M_{sr}]\}}{dt} \tag{2.68}$$

$$\begin{aligned}\left[V_{sdq0}\right] = {} & \{[T(\theta_s)][R_s][T(\theta_s)]^{-1}\}\left[I_{sdq0}\right] + \{[T(\theta_s)][L_s][T(\theta_s)]^{-1}\}\frac{d\left[I_{sdq0}\right]}{dt} \\ & + \{[T(\theta_s)][L_s][T(\theta_s)]^{-1}\}\left[I_{sdq0}\right] + \left\{[T(\theta_s)][M_{sr}]\left[T_{3Nr}(\theta_{ref})\right]^{-1}\right\}\frac{d\left[I_{rdq0}\right]}{dt} \\ & + \left\{[T(\theta_s)]\frac{d\left\{[M_{sr}]\left[T_{3Nr}(\theta_{ref})\right]^{-1}\right\}}{dt}\right\}\left[I_{rdq0}\right]\end{aligned} \tag{2.69}$$

Rotor part:

$$[V_r] = [R_r][I_{rk}] + \frac{d\{[I_{rk}][L_r]\}}{dt} + \frac{d\{[I_s][M_{rs}]\}}{dt} \tag{2.70}$$

$$\begin{aligned}\left[V_{rdq0}\right] = {} & \left\{\left[T(\theta_{ref})\right][R_r]\left[T(\theta_{ref})\right]^{-1}\right\}\left[I_{rdq0}\right] + \left\{\left[T(\theta_{ref})\right][L_r]\left[T(\theta_{ref})\right]^{-1}\right\}\frac{d\left[I_{rdq0}\right]}{dt} \\ & + \left\{\left[T(\theta_{ref})\right][M_{rs}][T(\theta_s)]^{-1}\right\}\left[I_{sdq0}\right] + \left\{\left[T(\theta_{ref})\right][M_{sr}]\left[T(\theta_{ref})\right]^{-1}\right\}\frac{d\left[I_{rdq0}\right]}{dt}\end{aligned} \tag{2.71}$$

By choosing a reference frame linked to the rotor, the angular relations can be written: $\theta_s = \theta_r$ and $\theta_{ref} = 0$

After the simplification we get Reduced size model of a healthy induction motor:

$$\begin{aligned}&\begin{bmatrix} L_{sc} & 0 & -\frac{N_r}{2}M_{sr} & 0 & 0 \\ 0 & L_{sc} & 0 & -\frac{N_r}{2}M_{sr} & 0 \\ -\frac{3}{2}M_{sr} & 0 & L_{rc} & 0 & 0 \\ 0 & -\frac{3}{2}M_{sr} & 0 & L_{rc} & 0 \\ 0 & 0 & 0 & 0 & L_e \end{bmatrix}\frac{d}{dt}\begin{bmatrix} I_{ds} \\ I_{qs} \\ I_{dr} \\ I_{qr} \\ I_e \end{bmatrix} \\ &= \begin{bmatrix} V_{ds} \\ V_{qs} \\ V_{dr} \\ V_{qr} \\ V_e \end{bmatrix} - \begin{bmatrix} R_s & -wL_{sc} & 0 & -w\frac{N_r}{2}M_{sr} & 0 \\ wL_{sc} & R_s & w\frac{N_r}{2}M_{sr} & 0 & 0 \\ 0 & 0 & R_r & 0 & 0 \\ 0 & 0 & 0 & R_r & 0 \\ 0 & 0 & 0 & 0 & R_e \end{bmatrix}\begin{bmatrix} I_{ds} \\ I_{qs} \\ I_{dr} \\ I_{qr} \\ I_e \end{bmatrix}\end{aligned} \tag{2.72}$$

With

$$L_{rc} = L_{rp} - M_{rr} + \frac{2L_e}{N_r} + 2L_e(1 - \cos(a)) \tag{2.73}$$

$$R_r = \frac{2R_e}{N_r} + 2R_{bs}(1 - \cos(a)) \tag{2.74}$$

The rotor fault matrix is expressed as:

$$[R_{rf}] = [R_r] + \begin{bmatrix} 0 & \cdots & \cdots & 0 & 0 & 0 & \cdots \\ \vdots & \cdots & \vdots & \vdots & \vdots & \vdots & \cdots \\ \vdots & \cdots & \vdots & \vdots & \vdots & \vdots & \cdots \\ \vdots & \cdots & \vdots & \vdots & \vdots & \vdots & \cdots \\ 0 & \cdots & 0 & 0 & 0 & 0 & \cdots \\ 0 & \cdots & 0 & R'_{bk} & -R'_{bk} & 0 & \cdots \\ 0 & \cdots & 0 & -R'_{bk} & R'_{bk} & 0 & \cdots \\ 0 & \cdots & 0 & 0 & 0 & 0 & \cdots \\ \vdots & \vdots & \vdots & \vdots & \vdots & 0 & \cdots \end{bmatrix} \tag{2.75}$$

The new matrix of rotor resistances becomes:

$$[R_{rfdq}] = [T(\theta_{ref})][R_{rf}][T(\theta_{ref})]^{-1} = [T(\theta_{ref})]\{[R_r] + [R'_r]\}[T(\theta_{ref})]^{-1} \tag{2.76}$$

With

$$[R_{rfdq}] = \begin{bmatrix} R_{rdd} & R_{rdq} \\ R_{rqd} & R_{rqq} \end{bmatrix} \tag{2.77}$$

The four terms are:

$$R_{rdd} = 2R_{bs}(1 - \cos(a)) + \frac{2R_e}{N_r} + \frac{2}{N_r}(1 - \cos(a)) \sum_k R_{bfk}(1 + \cos(2k - 1)a) \tag{2.78}$$

$$R_{rqq} = 2R_{bs}(1 - \cos(a)) + \frac{2R_e}{N_r} + \frac{2}{N_r}(1 - \cos(a)) \sum_k R_{bfk}(1 + \cos(2k - 1)a) \tag{2.79}$$

$$R_{rdq} = -\frac{2}{N_r}(1 - \cos(a)) \sum_k R_{bfk} \sin(2k - 1)a \tag{2.80}$$

$$R_{rqd} = -\frac{2}{N_r}(1 - \cos(a)) \sum_k R_{bfk} \sin(2k - 1)a \tag{2.81}$$

The index k refers to the broken bar.

For the mechanical part, after applying the transformation to the torque expression, we obtain:

$$C_{em} = \frac{3}{2}.p.N_r.M_{sr}[I_{ds}I_{qr} - I_{qs}I_{dr}] \tag{2.82}$$

II.5 Conclusion:

In this chapter, we explored the modeling of multi-winding systems in induction motors using the magnetically coupled electric circuits method. We began by introducing the fundamental principles of this modeling approach, emphasizing its importance in accurately representing the electrical and magnetic interactions within the motor.

A crucial aspect of this modeling process is the calculation of inductances, which we systematically analyzed for the stator, rotor, and the mutual inductance between them. These inductance values play a significant role in defining the dynamic behavior of the motor and its response to different operating conditions.

Building upon these inductance calculations, we established the governing equations for the stator and rotor circuits, as well as the mechanical equation that describes the motor's dynamic performance. These equations provide a mathematical framework for understanding the electrical and mechanical interactions within the system, facilitating both theoretical analysis and simulation-based studies.

Furthermore, we have presented the development of a multi-winding mathematical model that takes into consideration the rotor structure. The choice of such a model is driven by the objective of being able to simulate rotor bar breakage. This type of fault is modeled by an increase in the resistance of the defective element, allowing for a more accurate representation of its impact on motor performance.

Finally, we introduced the concept of a reduced-size model, which simplifies the full mathematical representation while preserving essential dynamic characteristics. This reduced model is particularly useful for computational efficiency in simulations and control system design.

The next chapter, we will present the simulation results obtained using both the complete and the reduced size model.

Chapter III: Simulation of multi-winding system

III.1 Introduction:

This chapter explores the simulation of the multi-winding model using both the full and reduced models, enabling the representation of various graphs related to stator current, rotor bars current, end ring current, d-q components current, torque, and speed. The simulation is conducted under different operating conditions, including a healthy state, a single broken bar, and multiple adjacent and sperate broken bars.

III.2 Simulation of the model:

The simulation of both the full and reduced models is conducted in MATLAB using the Fourth-Order Runge-Kutta Method (Runge-Kutta ODE4). This method enables the simulation of both healthy and faulty rotor bar conditions. To simulate rotor faults, the initial resistance value of the broken bars is replaced with a finite value, a technique known as the finite resistance method. Increasing the bar resistance by a factor of 11 produces results that align with experimental findings [1]. In our study, we adopted the same approach, considering an 11-fold increase in the initial bar resistance. However, for a step size of 10^{-3}s, increasing the resistance beyond this threshold leads to numerical instability in our model.

III.3 Full model:

In the simulation diagram shown in Figure III.1, three distinct blocks are present:

- A mechanical block, which represents the equation of motion (2.63).
- An electrical block, which corresponds to (2.72).
- An electromechanical block, which represents the torque equation (2.62).

The block diagram used for the simulation is as follows:

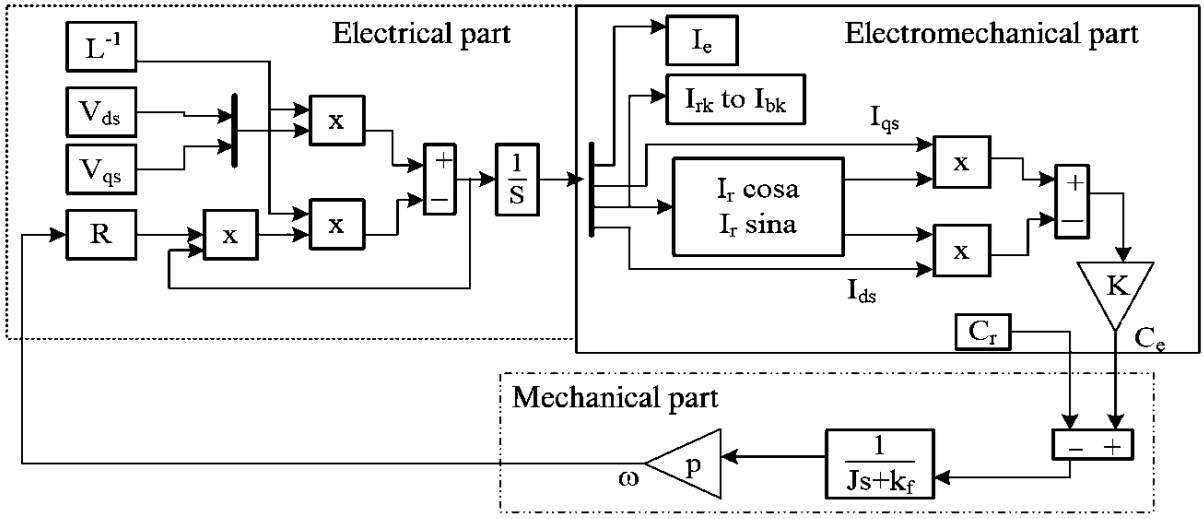


Figure III.1. Simulink schematic of complete model.

III.3.1 Healthy machine case no-load conditions:

The simulation involves starting the machine under no-load conditions with full voltage applied. During the simulation, the speed and phase current are recorded. Detecting faults in the machine is challenging when it operates without a load.

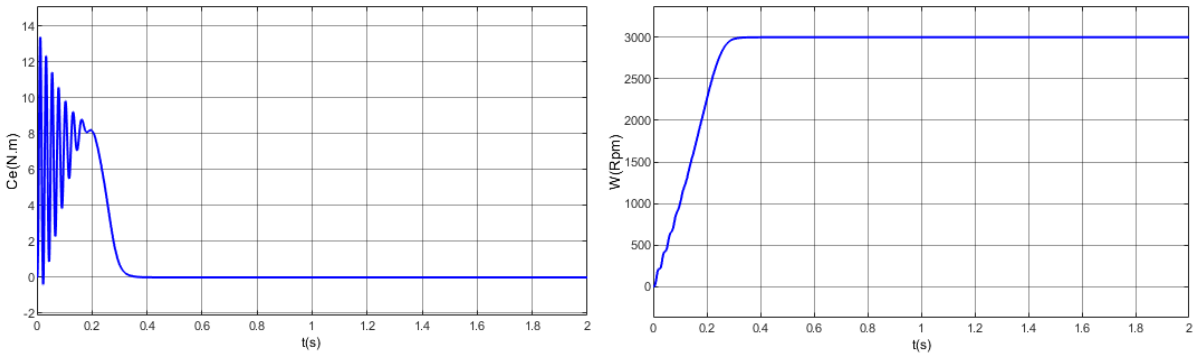
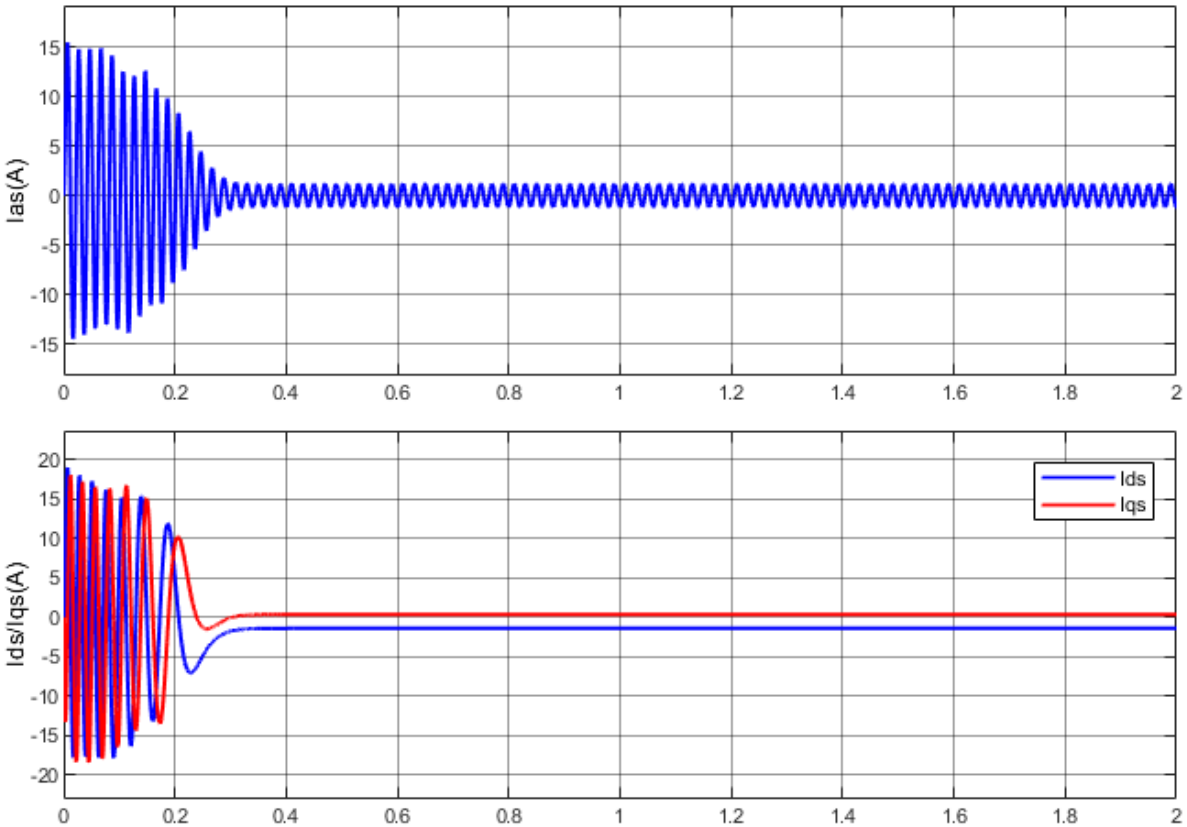


Figure III.2. Electromagnetic torque and rotation speed in healthy machine case no-load conditions.



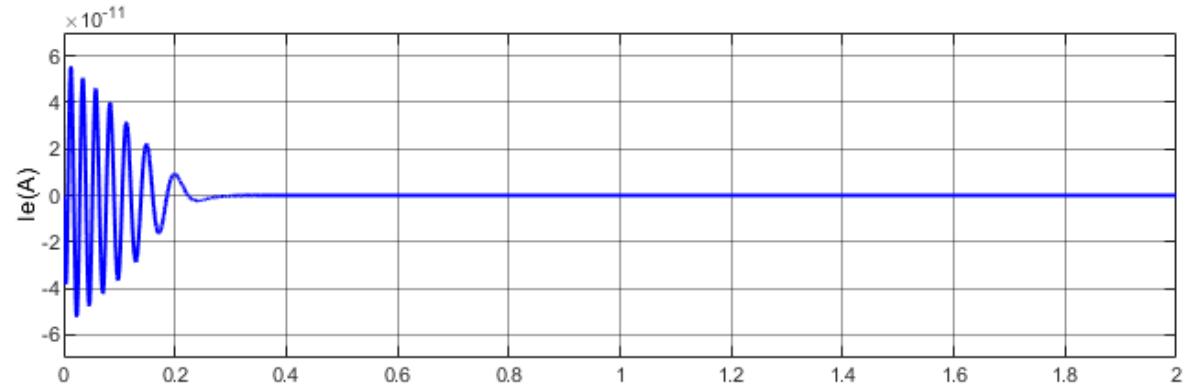
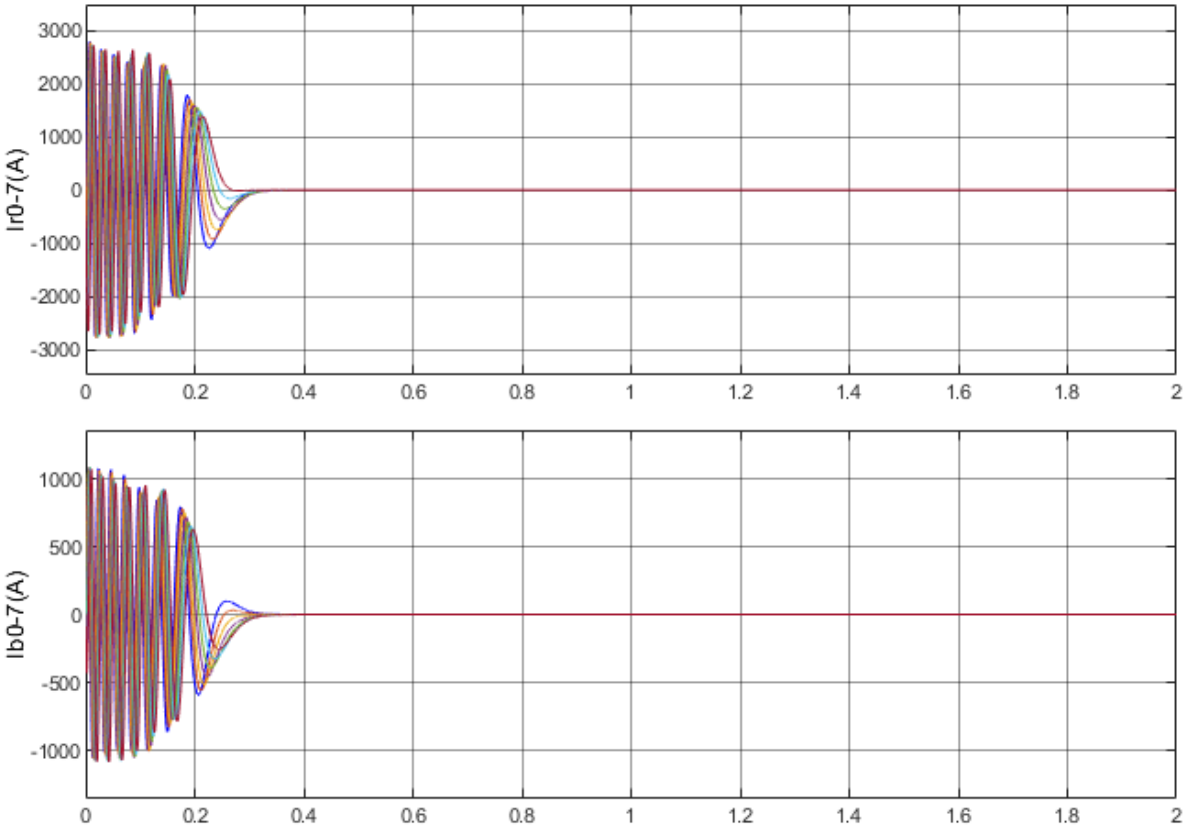


Figure III.3. Phase a current, I_{ds}/I_{qs} current and end ring current in healthy machine case no-load conditions.



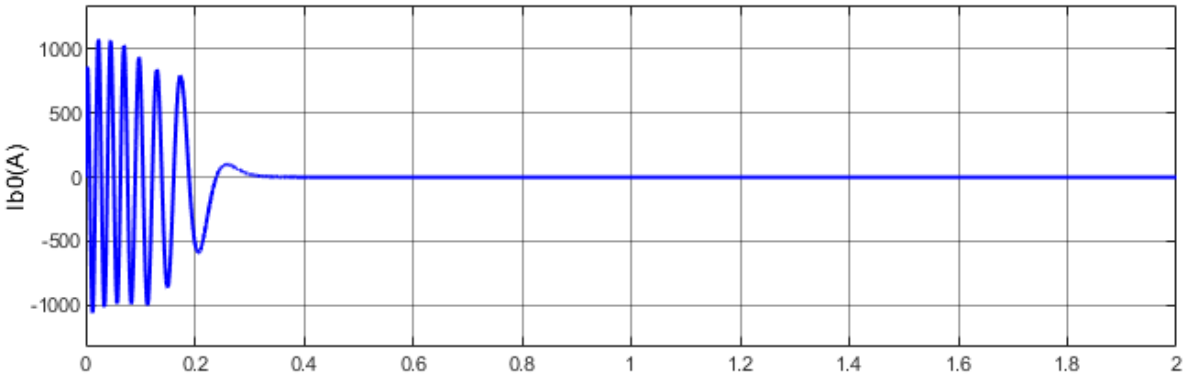


Figure III.4. Current of ring portions 0 to 7, current of bar 0 to 7 and current of bar 0 in healthy machine case no-load conditions.

III.3.2 Result interpretation:

Initially, the machine operates without an applied load torque, meaning it runs under no-load conditions. Figure III.2 depicts the time evolution of rotational speed during both the transient and steady-state phases. Following an initial transient response, the speed stabilizes near the synchronous speed, which is expected due to the absence of load torque. The figure also illustrates the electromagnetic torque behavior, which, after an initial transient phase, settles at a value close to zero, as no external load is applied.

Figure III.3 presents the time evolution of the stator current, I_{ds}/I_{qs} and end ring current under no-load conditions, showing its behavior during both transient and steady states. Similarly, Figure III.4 displays the rotor ring and bar currents denoted as I_{r0} to I_{r7} and I_{b0} to I_{b7} over time. It can be observed that, despite the absence of load torque, the rotor bars carry small but nonzero currents in steady state. This residual current is attributed to the influence of harmonic fields. Since these harmonic fields do not rotate exactly at synchronous speed, they induce fluctuating electromagnetic effects, leading to weak but measurable currents in the rotor loop, since viscous friction is assumed zero, it does not generate resistive torque thus it doesn't contribute to the current in the bars.

III.3.3 Healthy machine case with load:

During this simulation, a load of 3.5 N.m is applied to the machine at time t = 0.6 s. This torque represents the nominal torque of the machine under study.

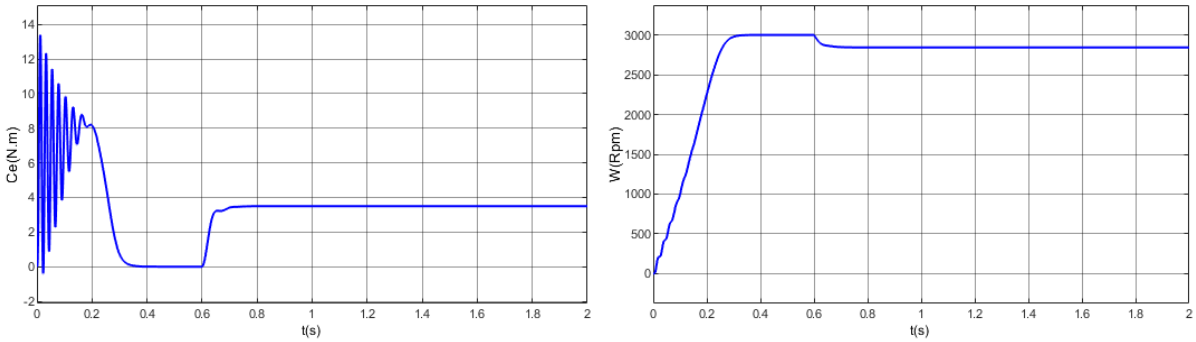
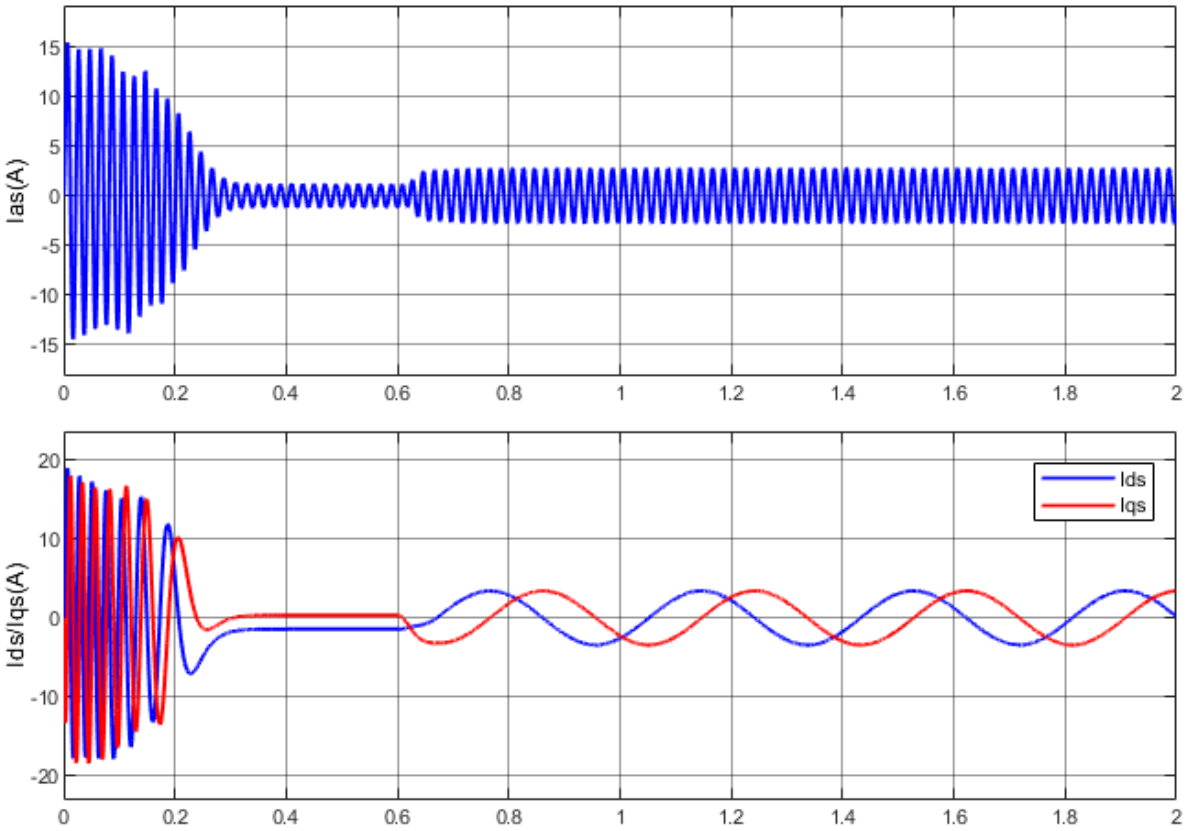


Figure III.5. Electromagnetic torque and rotation speed in healthy machine case with load.



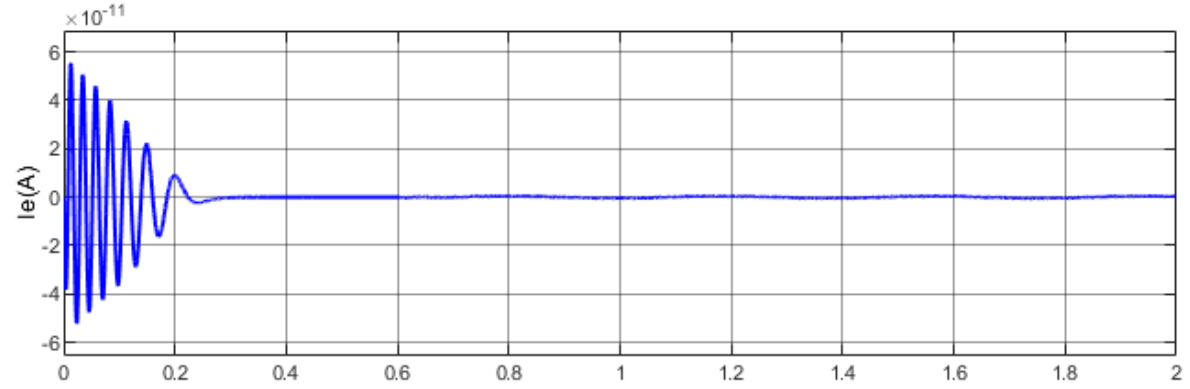
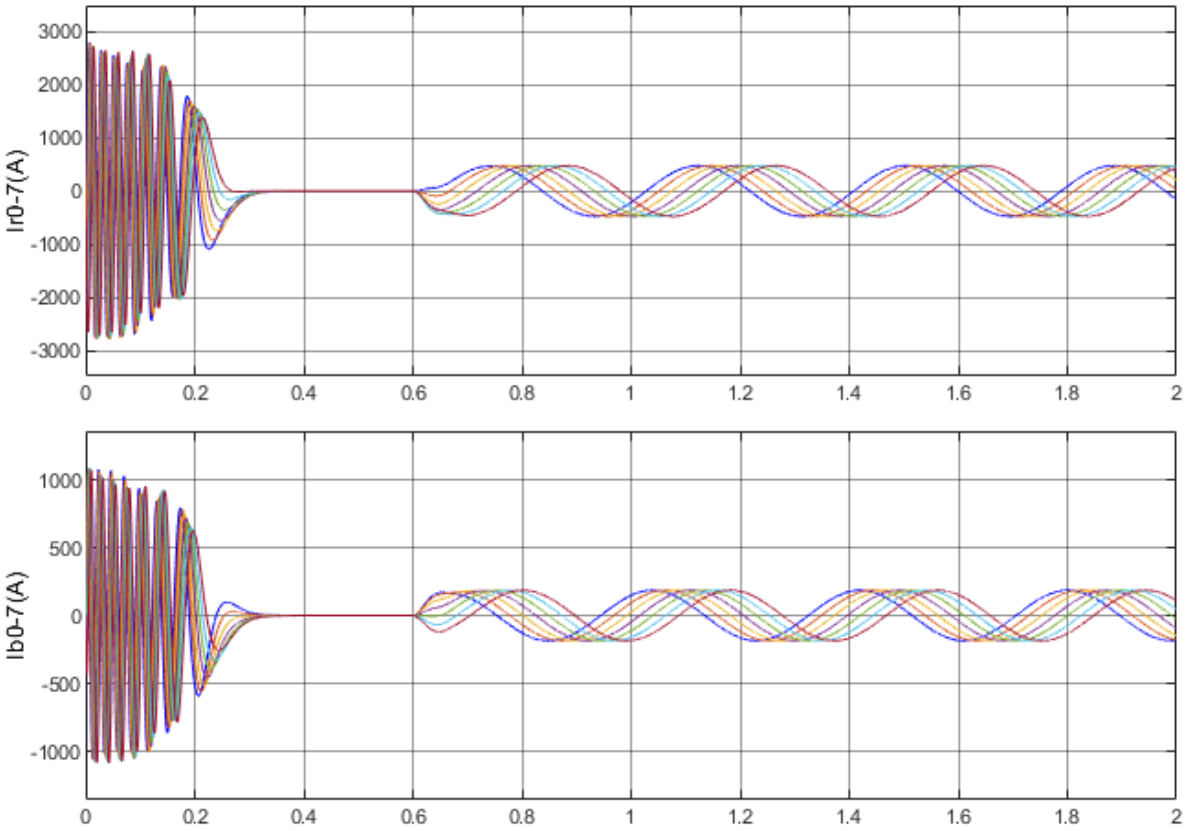


Figure III.6. Phase a current, I_{ds}/I_{qs} current and end ring current in healthy machine case with load.



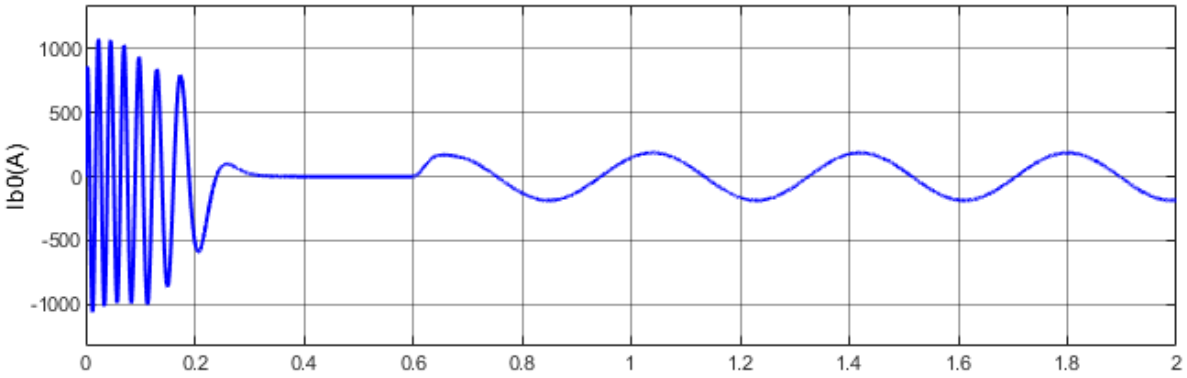


Figure III.7. Current of ring portions 0 to 7, current of bar 0 to 7 and current of bar 0 in healthy machine case with load.

III.3.4 Result interpretation:

When a load torque of 3.5 N·m is applied at t=0.6s, the machine transitions to operating under load conditions. Figure III.5 presents the time evolution of the rotational speed during both the transient and steady-state phases. After an initial transient response, the speed stabilizes at 2842 rpm. The figure also illustrates the electromagnetic torque, which, following a transient phase, settles at approximately 3.5N·m, as expected under the applied load.

Figure III.6 shows the stator, I_{ds}/I_{qs} and end ring current time evolution in the presence of a 3.5N·m load torque, highlighting its behavior in both transient and steady-state conditions. Similarly, Figure III.7 depicts the rotor bar and ring currents I_{r0} to I_{r7} and I_{b0} to I_{b7} over time. It is observed that, in steady state, the rotor bars carry currents at a fundamental frequency ($g.f_s$), which aligns with theoretical expectations. These currents maintain the same fundamental frequency in steady-state operation, reflecting the rotor's response to the applied load torque.

III.3.5 One broken case no-load condition:

This simulation involves starting the machine under no-load conditions with full voltage applied, at t=1s b_0 becomes broken.

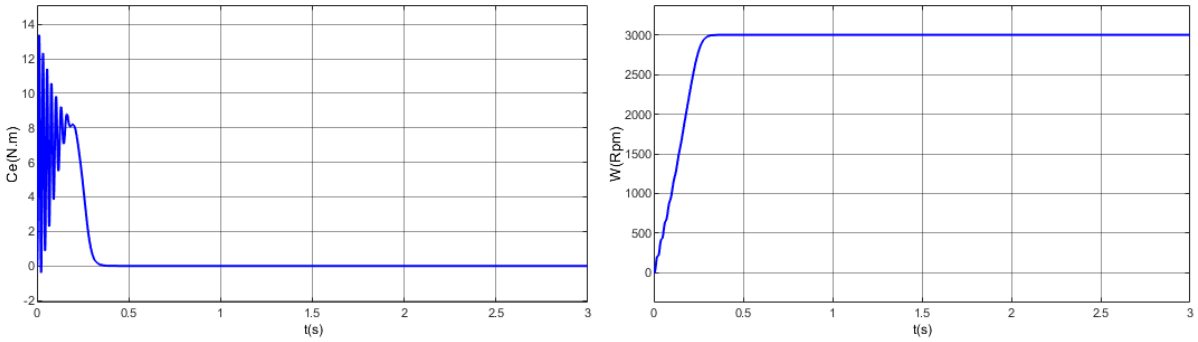
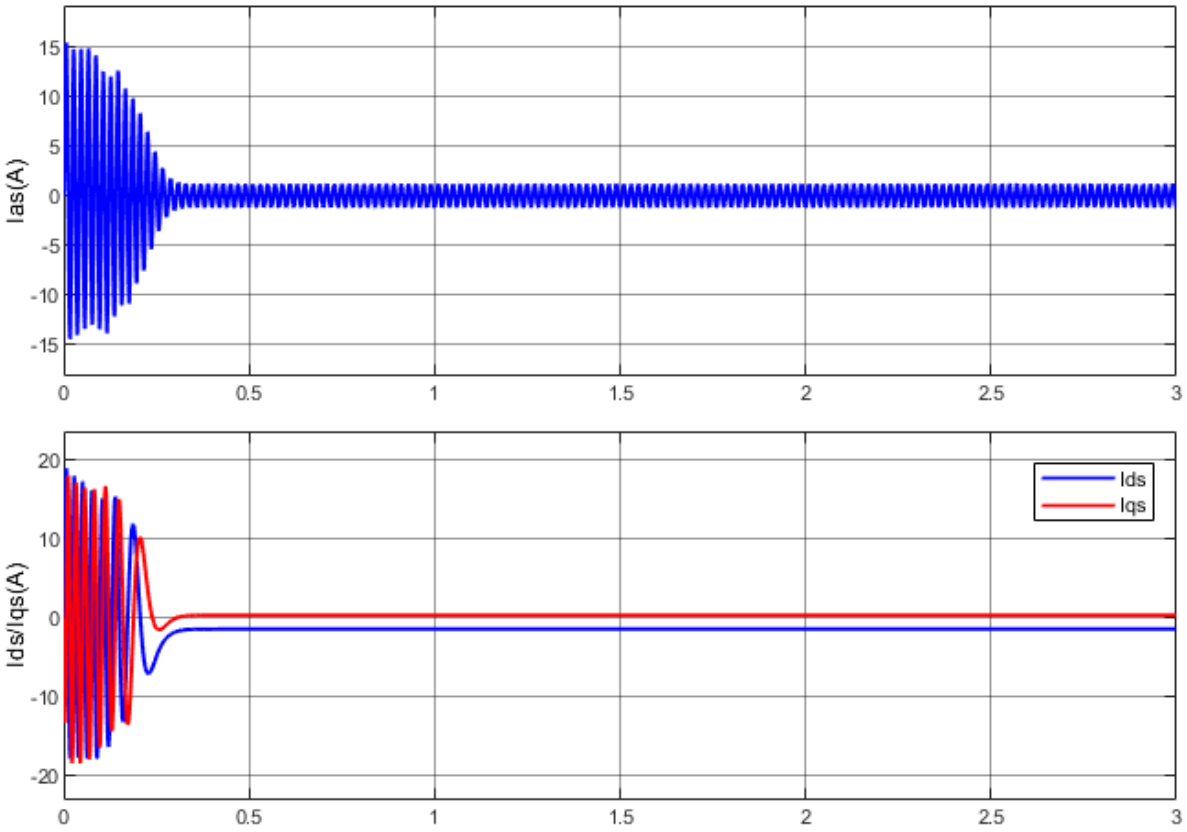


Figure III.8. Electromagnetic torque and rotation speed in one broken bar case no-load condition.



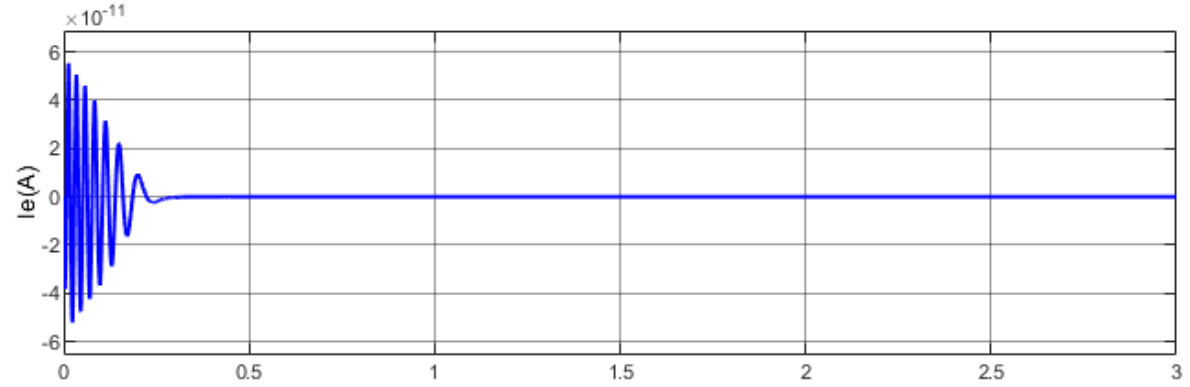
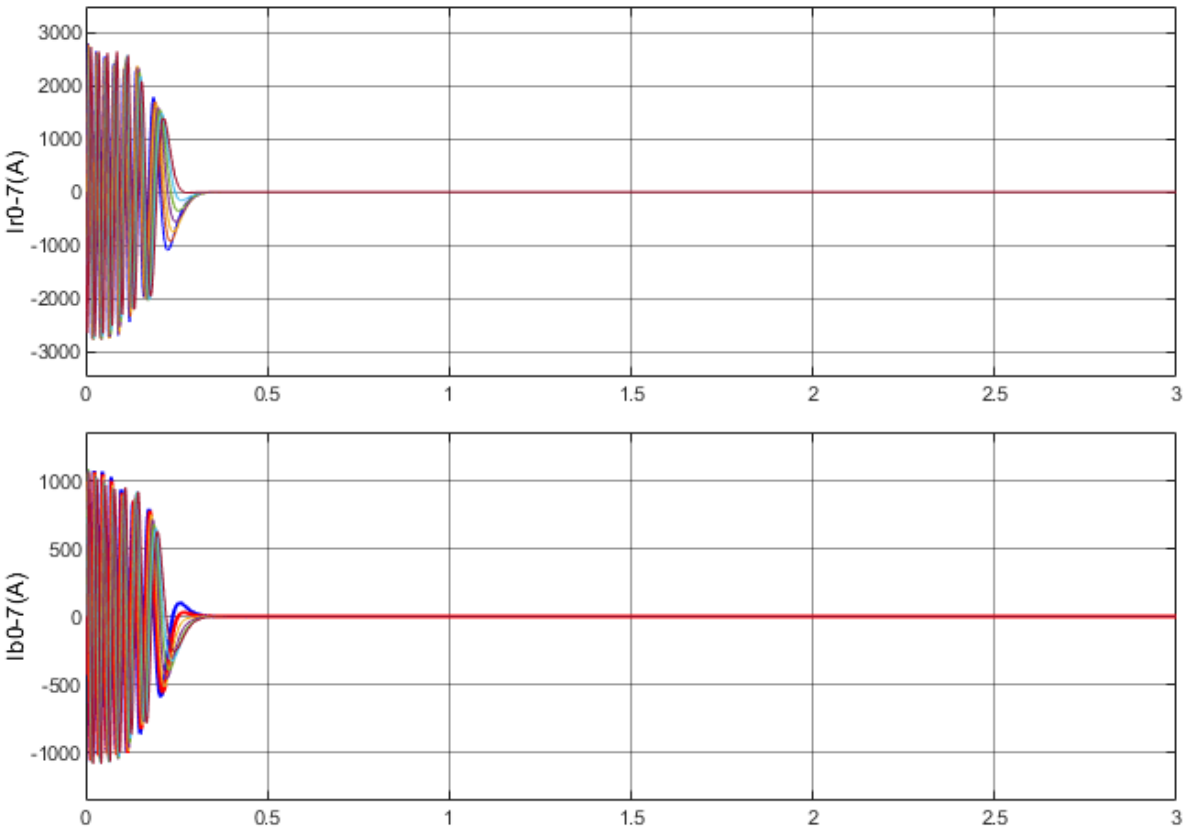


Figure III.9. Phase a current, I_{ds}/I_{qs} current and end ring current in one broken bar case no-load condition.



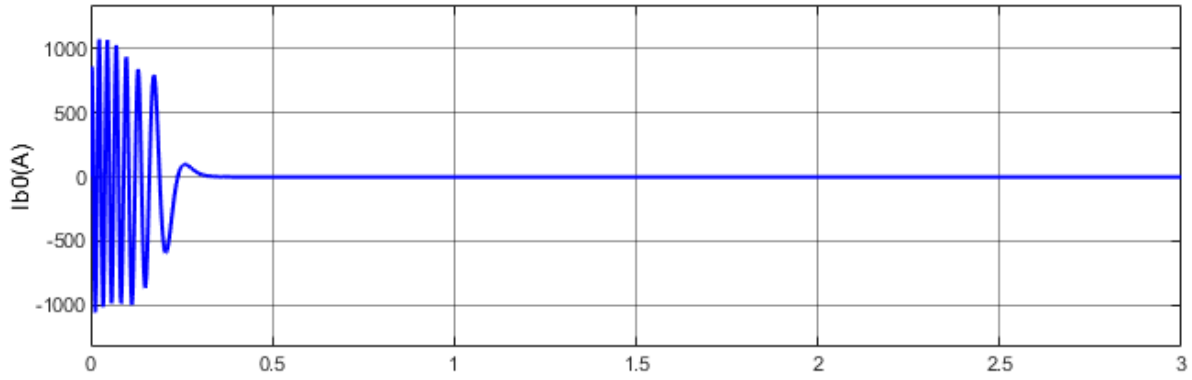


Figure III.10. Current of ring portions 0 to 7, current of bar 0 to 7 and current of bar 0 in one broken bar case no-load condition.

III.3.6 Result interpretation:

Initially, the machine operates without an applied load torque, meaning it runs under no-load conditions. Figure III.8 illustrates the time evolution of rotational speed during both the transient and steady-state phases when a bar break (b_0) occurs at t = 1s. Following the transient phase, the speed stabilizes near the synchronous speed, as expected due to the absence of load torque. The figure also depicts the evolution of the electromagnetic torque (C_{em}), which, after a transient response, settles at a value close to zero, consistent with the no-load condition.

Figure III.9 presents the time evolution of the stator, I_{ds}/I_{qs} and end ring current in both transient and steady-state conditions, showing that there are no significant effects of the bar break under no load. Similarly, Figure III.10 displays the rotor bar and ring currents I_{r0} to I_{r7} and I_{b0} to I_{b7} over time, highlighting their behavior in response to the fault. It is observed that under no-load conditions, the fault signatures in the rotor remain minimal, indicating a relatively weak impact of the bar break when no external torque is applied.

Detecting faults in the machine is challenging when it operates without a load.

III.3.7 One broken bar case with load:

This simulation involves starting the machine under no-load conditions, then at t=0.6 a load of 3.5 N.m is applied, at t=1s b_0 becomes broken.

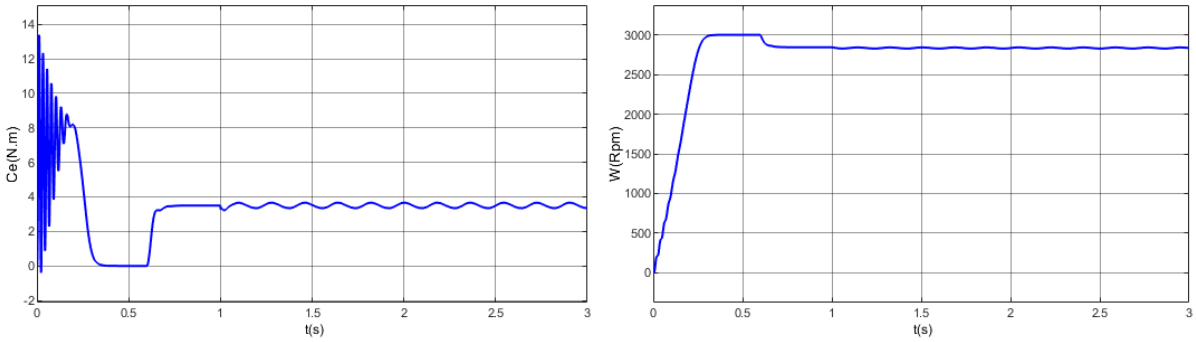
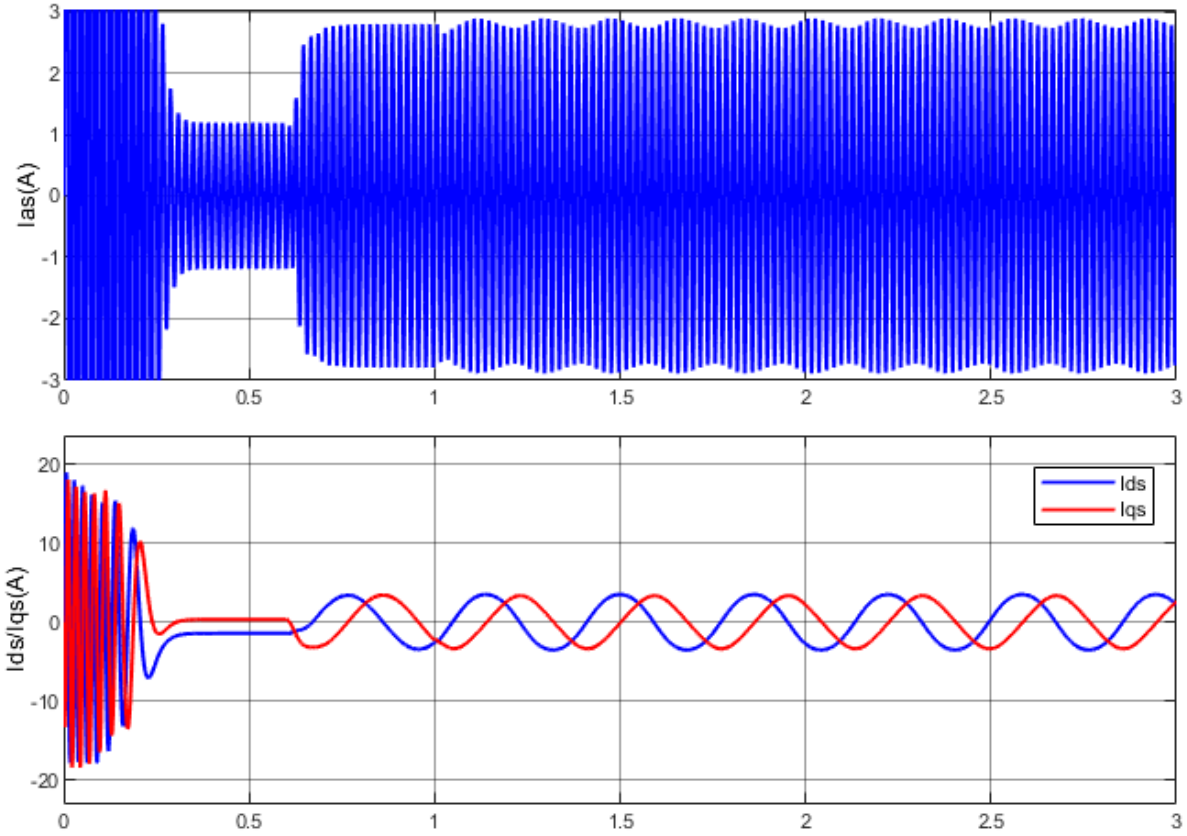


Figure III.11. Electromagnetic torque and rotation speed in one broken bar case with load.



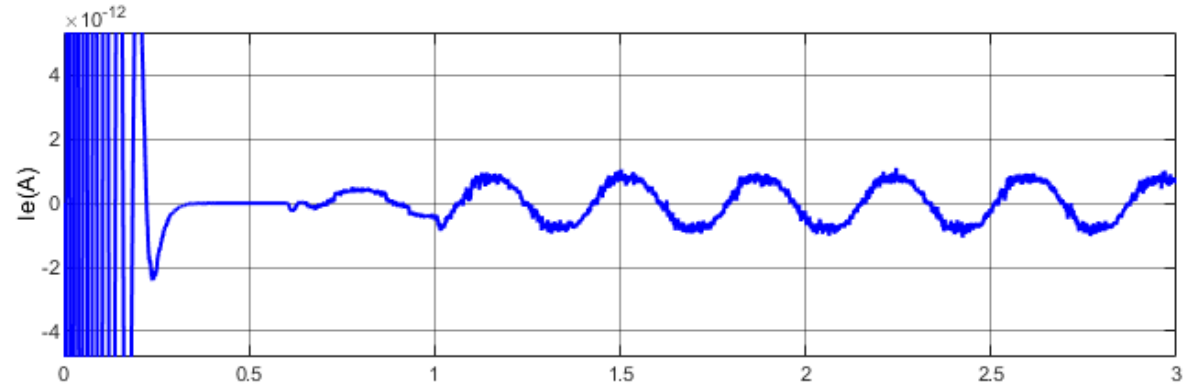
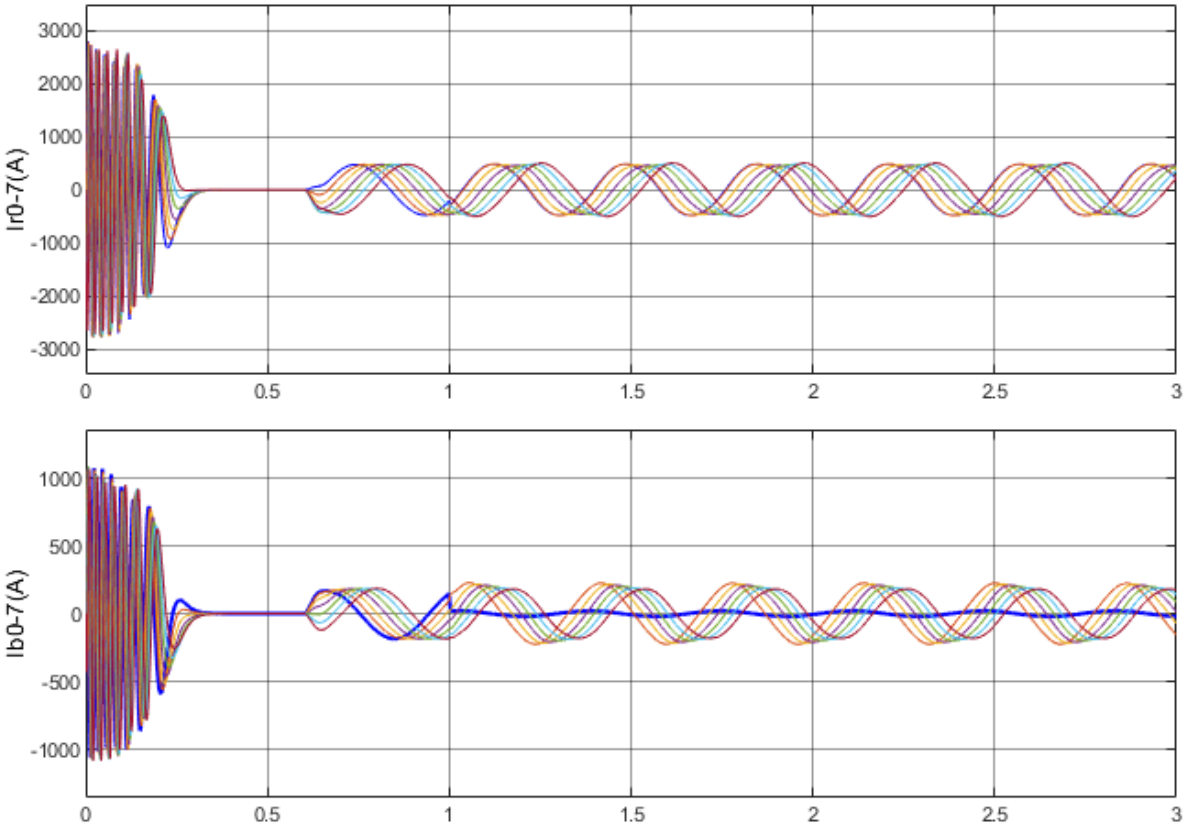


Figure III.12. Phase a current, I_{ds}/I_{qs} current and end ring current in one broken bar case with load.



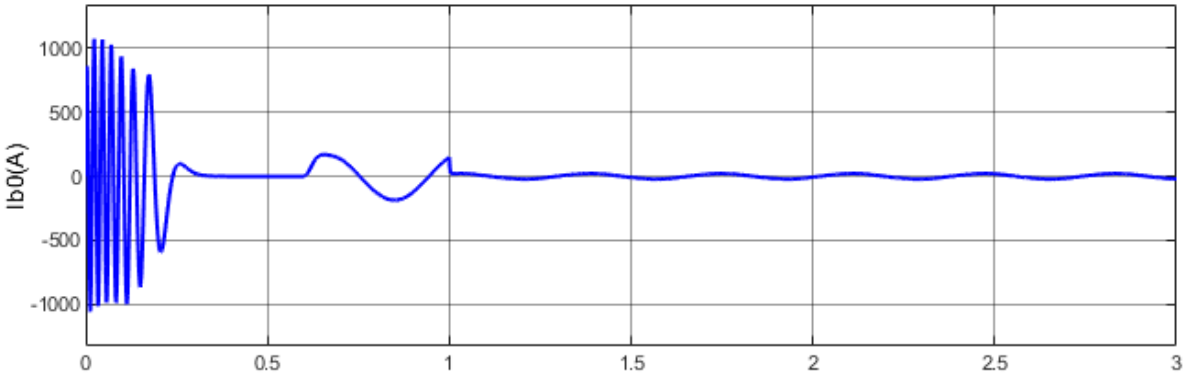


Figure III.13. Current of ring portions 0 to 7, current of bar 0 to 7 and current of bar 0 in one broken bar case with load.

III.3.8 Result interpretation:

When a load torque of 3.5N·m is applied at t = 0.6s, the machine begins operating under load conditions. Figure III.11 illustrates the time evolution of rotational speed during both transient and steady-state phases, where the speed oscillates at a frequency of ($2 \cdot g \cdot f_s$) around 2842 rpm. The figure also depicts the electromagnetic torque (C_{em}) in the presence of a bar break (b_0) at t = 1s. After an initial transient phase, the torque oscillates at a frequency of ($2 \cdot g \cdot f_s$) around approximately 3.5N·m.

Figure III.12 presents the time evolution of the stator, I_{ds}/I_{qs} and end ring current under transient and steady-state conditions in the presence of the bar break (b_0) at t = 1s. Similarly, Figure III.13 illustrates the rotor bar currents I_{r0} to I_{r7} and I_{b0} to I_{b7} under the same conditions. It is observed that the currents flowing in the adjacent bars significantly exceed their nominal values. This redistribution of electrical and thermal stresses onto the neighboring conductors increases the risk of failure in these components.

The following observations can be made after the breakage of the bar at t = 1s:

- The speed decreases to an average oscillating value of 2834 rpm, and the electromagnetic torque adjusts to counterbalance the resistive torque showing oscillations at a frequency of ($2 \cdot g \cdot f_s$) as well.
- Speed fluctuations appear as a result of this structural defect.
- The stator phase currents remain 120° out of phase with each other, but a ripple in their amplitude emerges due to the bar breakage, as illustrated in Figure III.12.

Additionally, the rotor, now affected by this structural defect, generates not only a direct rotor field rotating at ($g.\omega_s$) relative to the rotor but also a reverse field rotating at ($-g.\omega_s$) in the rotor reference frame. The interaction between these rotor fields and the stator winding produces an

electromagnetic torque composed of a constant direct component and a sinusoidal reverse component with a pulsation of ($2.g.\omega_s$). This interaction ultimately leads to speed oscillations.

III.3.9 Two adjacent broken bars with load:

This simulation involves starting the machine under no-load conditions, then at t=0.6 a load of 3.5 N.m is applied, at t=1s b_0 becomes broken and at t=1.5s b_1 is broken.

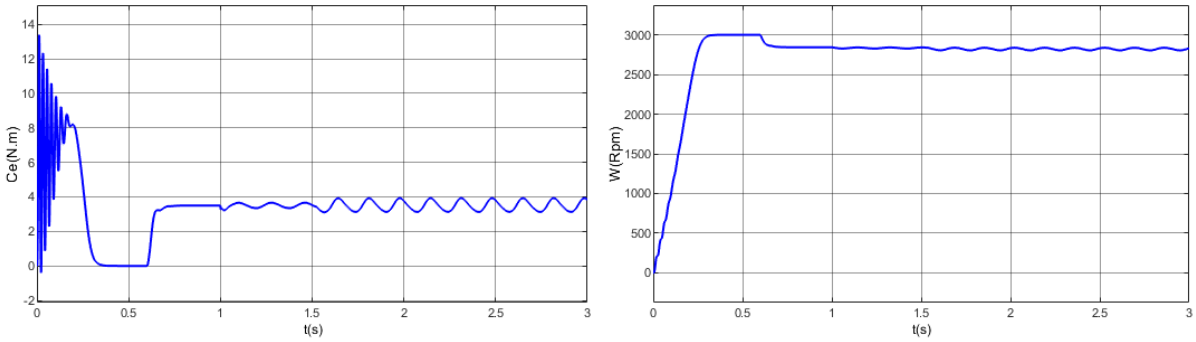
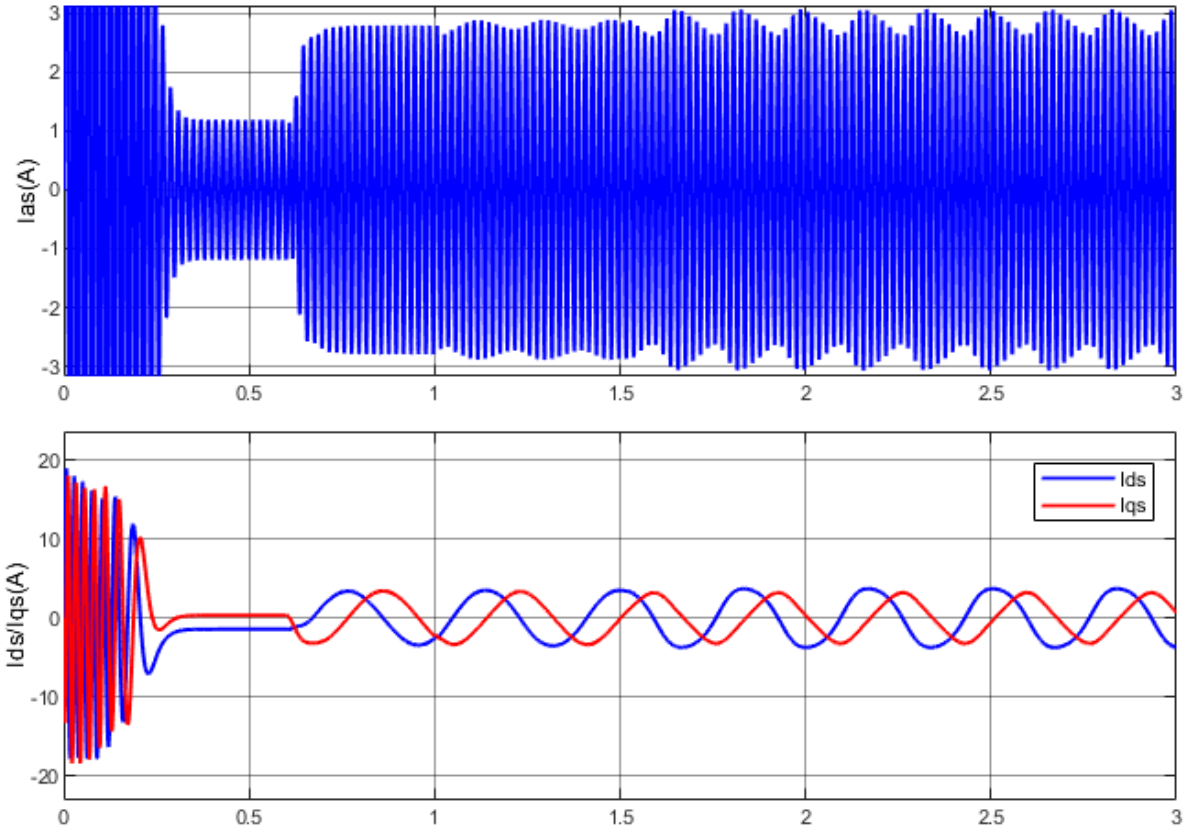


Figure III.14. Electromagnetic torque and rotation speed in two adjacent broken bars case with load.



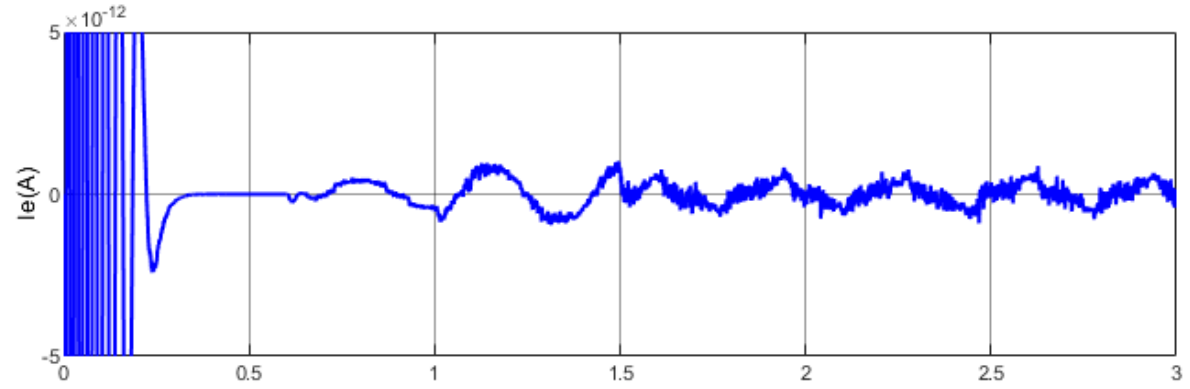
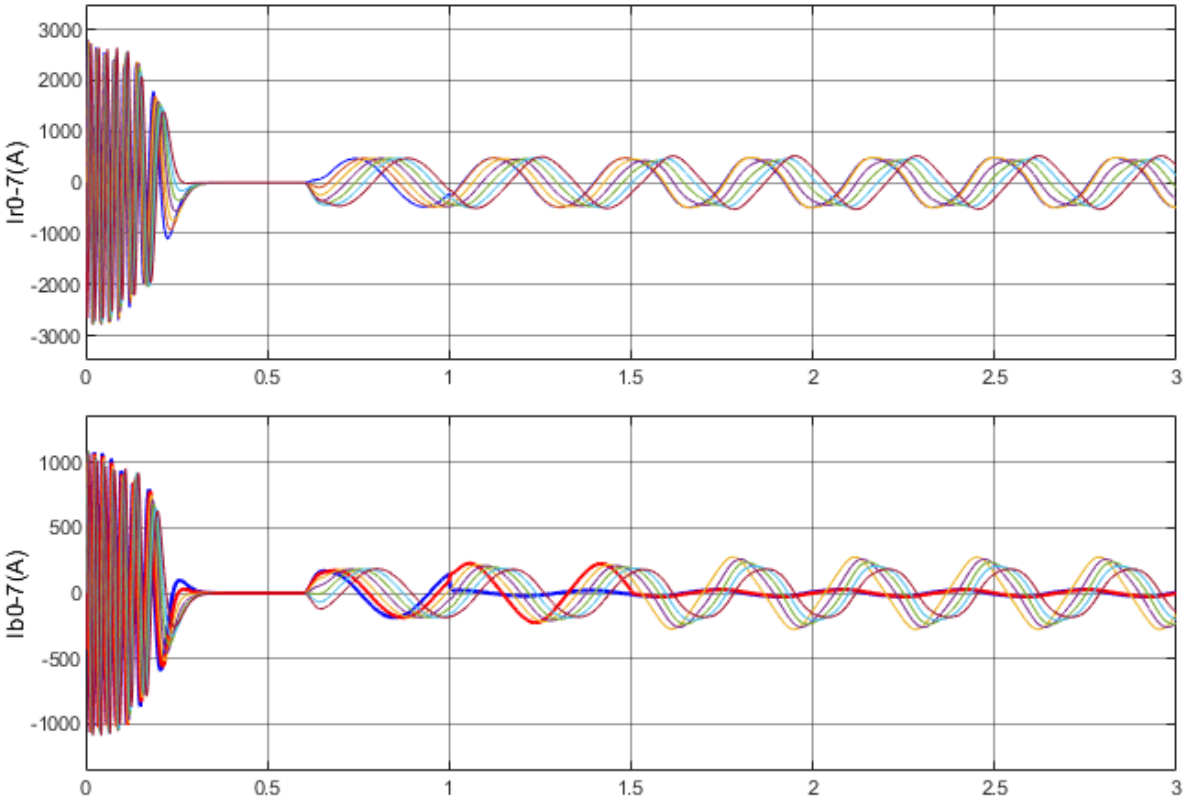


Figure III.15. Phase a current, I_{ds}/I_{qs} current and end ring current in two adjacent broken bars case with load.



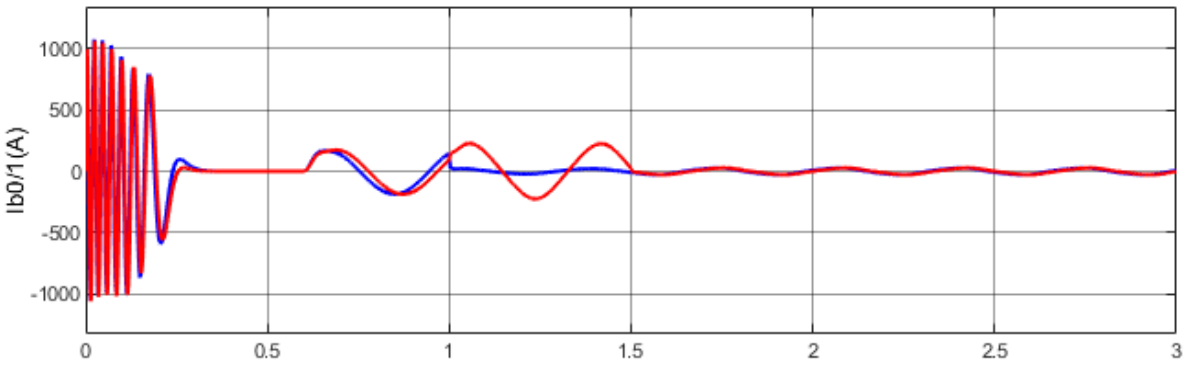


Figure III.16. Current of ring portions 0 to 7, current of bar 0 to 7 and current of bar 0 in two adjacent broken bars case with load.

III.3.10 Result interpretation:

When a load torque of 3.5N·m is applied at t = 0.6s, the machine transitions to operating under load conditions. Figure III.14 illustrates the time evolution of the electromagnetic torque (C_{em}) during both transient and steady-state conditions in the presence of a bar break (b_0) at t = 1s and (b_1) at t = 1.5s. After the initial transient phase, the torque stabilizes at approximately 3.5N·m. However, after the first bar breakage oscillations appear in the electromagnetic torque at a frequency of ($2.g.f_s$), and increase in amplitude after the second bar breakage.

Figure III.15 presents the time evolution of the stator, I_{ds}/I_{qs} and end ring current under transient and steady-state conditions when the bar breaks occur (b_0) at t = 1s and (b_1) at t = 1.5s. Similarly, Figure III.16 illustrates the rotor bar currents I_{r0} to I_{r7} and I_{b0} to I_{b7} under the same conditions. It is observed that the currents in the bars adjacent to the broken ones significantly exceed their nominal values, and the current of the broken bars is very small.

The severity of bar breakage effects, particularly the oscillations in rotational speed (ω_r) and electromagnetic torque (C_{em}), increases as the number of broken bars grows. The following key observations are made:

- Greater oscillation amplitude: As more bars break, the oscillations become more pronounced, which accelerates machine deterioration.
- Proportional increase in stator current amplitude: The stator current amplitude grows in relation to the number of broken bars.
- Current redistribution: When a rotor fault occurs, the currents in the broken bars decrease to nearly zero, while the currents in the adjacent bars become significantly unbalanced. The electrical load previously carried by the broken bars is redistributed to the neighboring bars, leading to increased stress on these components.

III.4 Reduced model:

Similar to the full model three distinct blocks are present shown in Figure III.17:

- A mechanical block, which represents the equation of motion (2.63).
- An electrical block, which corresponds to (2.72).
- An electromechanical block, which represents the torque equation (2.82).

The block diagram used for the simulation is as follows:

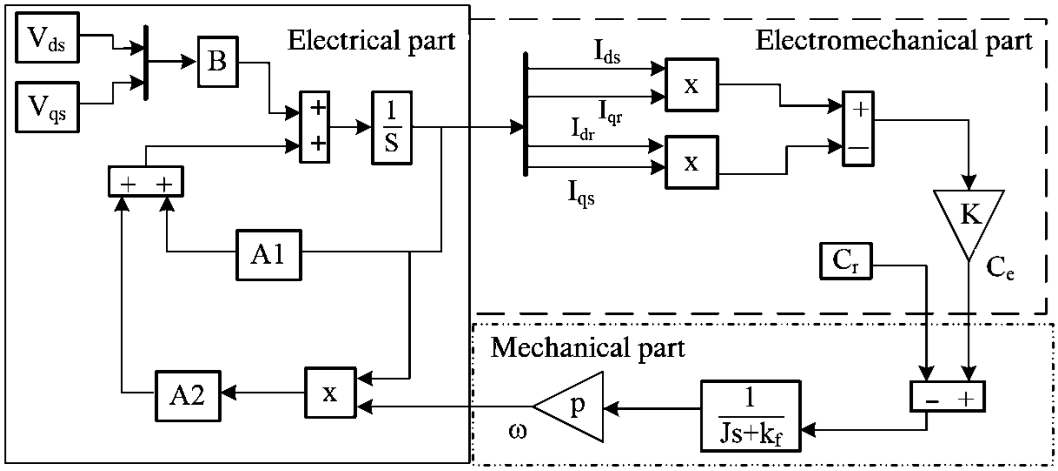


Figure III.17. Simulink schematics of reduced model.

The matrix representing inductances is:

$$[L] = \begin{bmatrix} L_{sc} & 0 & -\frac{N_r}{2}M_{sr} & 0 & 0 \\ 0 & L_{sc} & 0 & -\frac{N_r}{2}M_{sr} & 0 \\ -\frac{3}{2}M_{sr} & 0 & L_{rc} & 0 & 0 \\ 0 & -\frac{3}{2}M_{sr} & 0 & L_{rc} & 0 \\ 0 & 0 & 0 & 0 & L_e \end{bmatrix} \quad (3.1)$$

With

$$[B] = [L^{-1}]$$

Matrice A is defined as follows:

$$[A] = \left[[A_1] + w[A_2]\right][B] \quad (3.2)$$

With

$$[A_1] = \begin{bmatrix} R_s & 0 & 0 & 0 & 0 \\ 0 & R_s & 0 & 0 & 0 \\ 0 & 0 & R_{rdd} & R_{rdq} & 0 \\ 0 & 0 & R_{rqd} & R_{rqq} & 0 \\ 0 & 0 & 0 & 0 & R_e \end{bmatrix}$$

And

$$[A_2] = \begin{bmatrix} 0 & -L_{sc} & 0 & -\frac{N_r}{2}M_{sr} & 0 \\ L_{sc} & 0 & \frac{N_r}{2}M_{sr} & 0 & 0 \\ 0 & 0 & 0 & 0 & 0 \\ 0 & 0 & 0 & 0 & 0 \\ 0 & 0 & 0 & 0 & 0 \end{bmatrix}$$

III.4.1 Healthy machine case no-load conditions:

The test involves starting the machine under no-load conditions with full voltage applied. During the test, the speed and phase current are recorded.

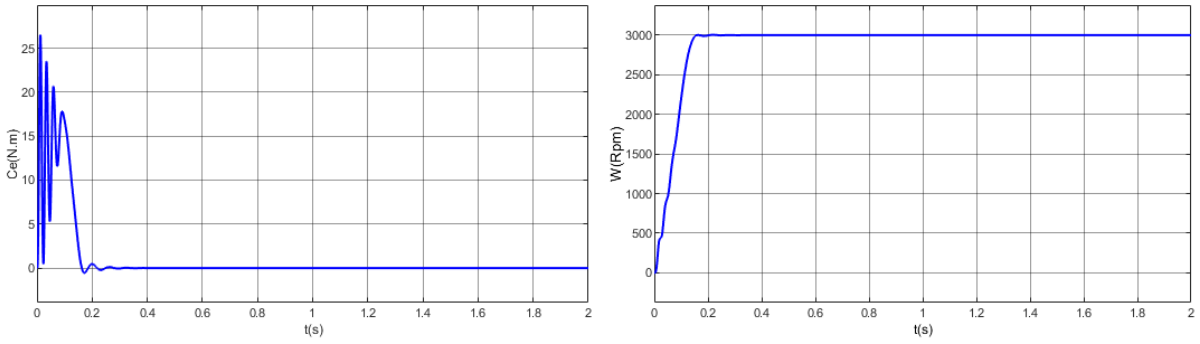


Figure III.18. Electromagnetic torque and rotation speed in healthy machine case no-load conditions.

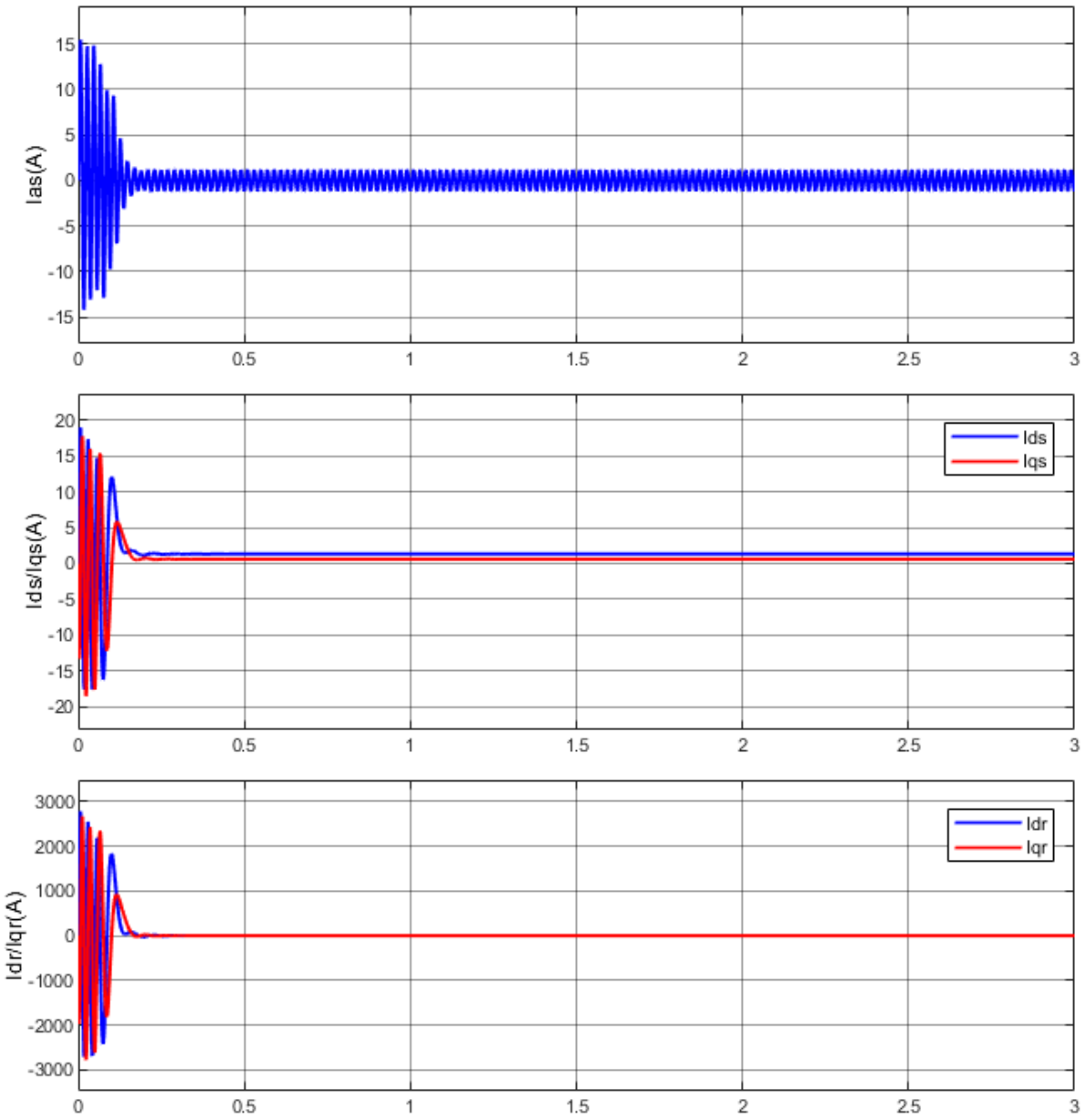


Figure III.19. Phase a current, I_{ds}/I_{qs} and I_{dr}/I_{qr} currents in healthy machine case no-load conditions.

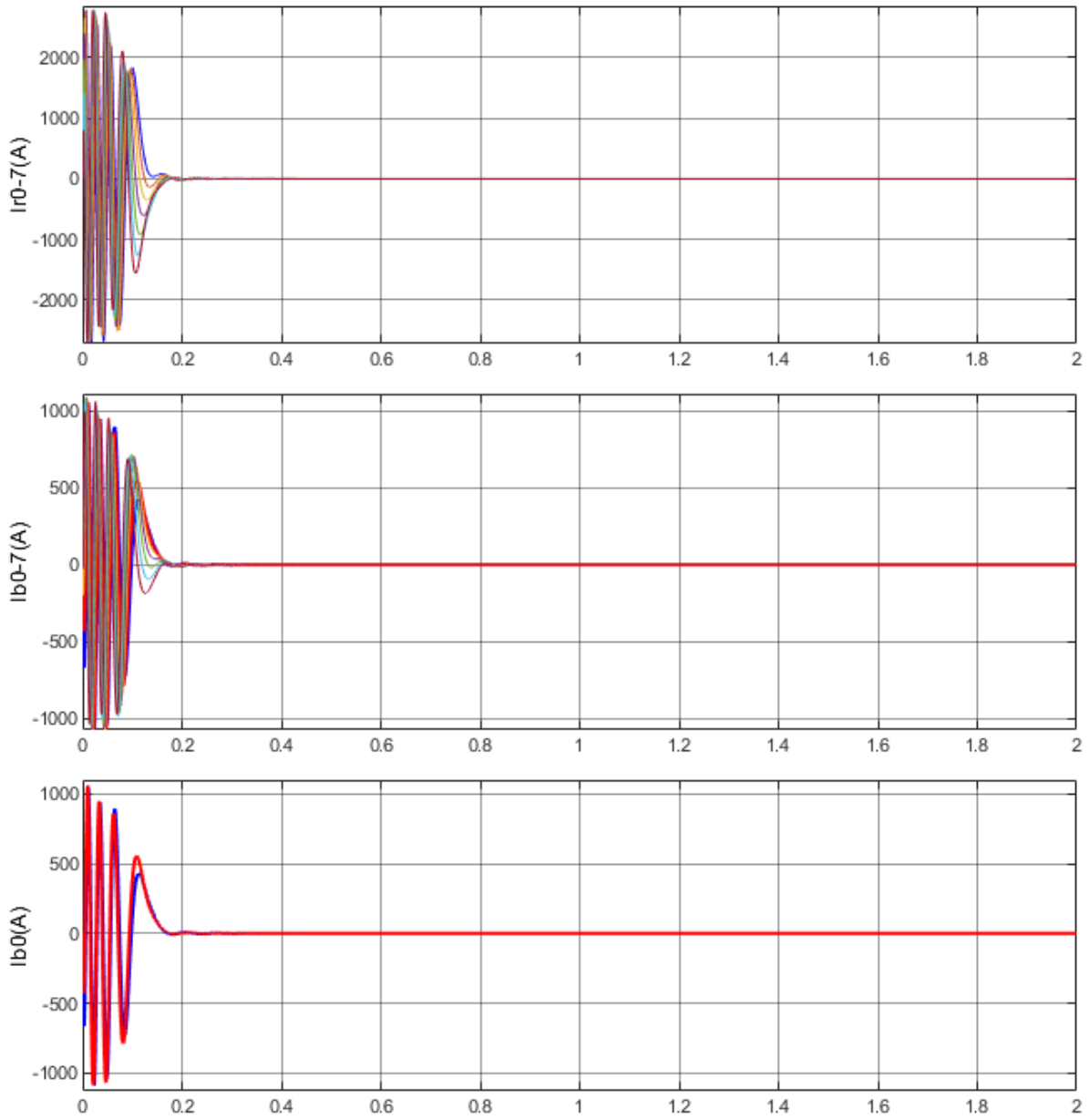


Figure III.20. Current of ring portions 0 to 7, current of bar 0 to 7 and current of bar 0 in healthy machine case no-load conditions.

III.4.2 Healthy machine case with load:

In this simulation a load of 3.5 N.m is applied to the machine at time t = 0.6 s.

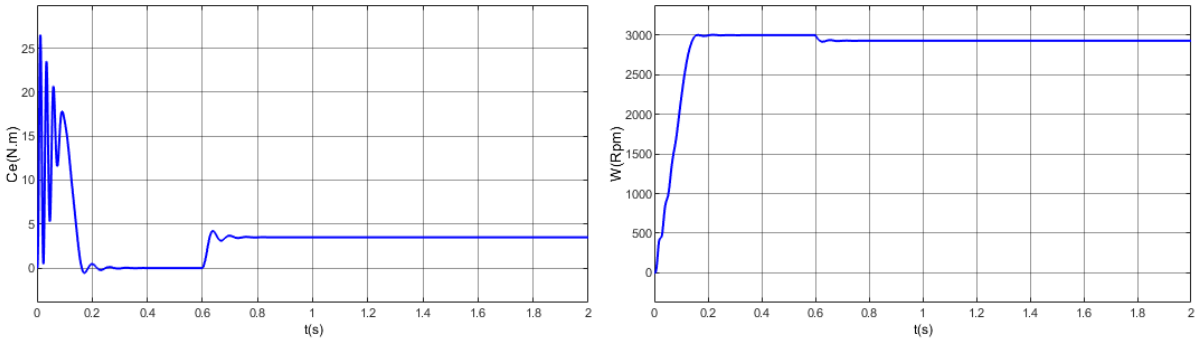
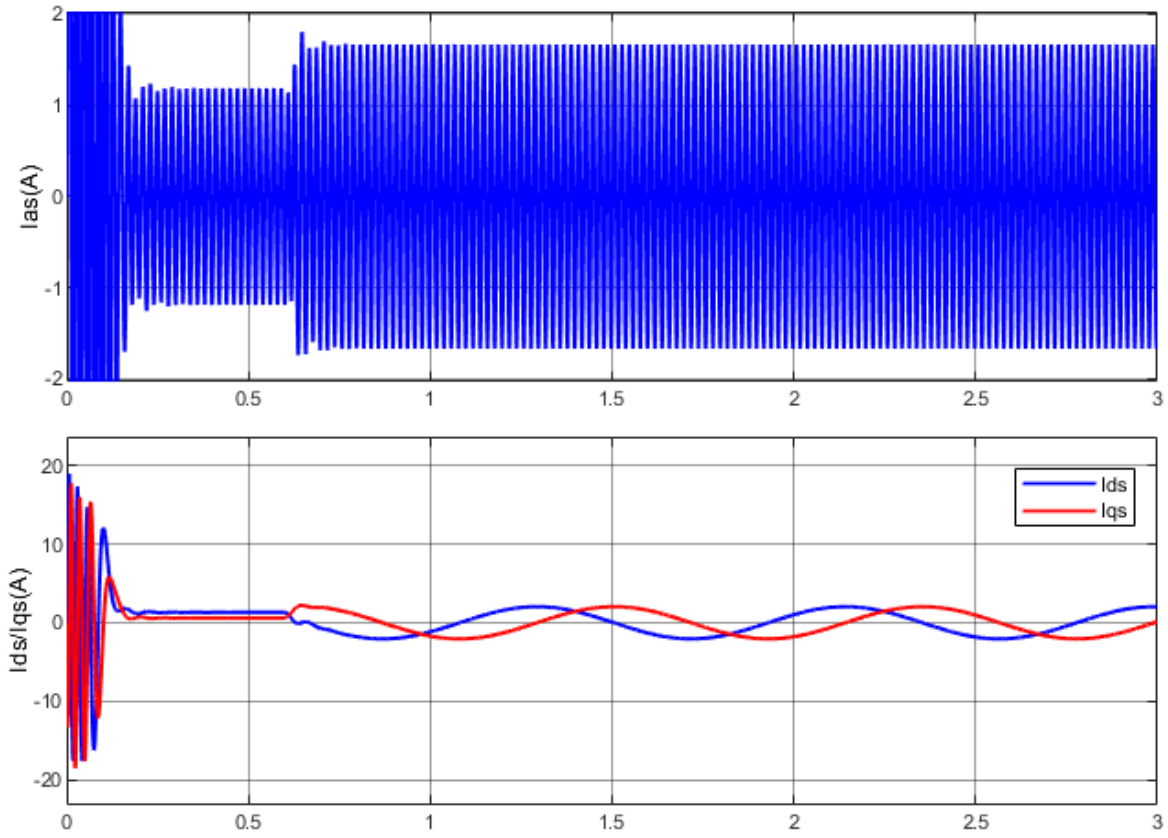


Figure III.21. Electromagnetic torque and rotation speed in healthy machine case with load.



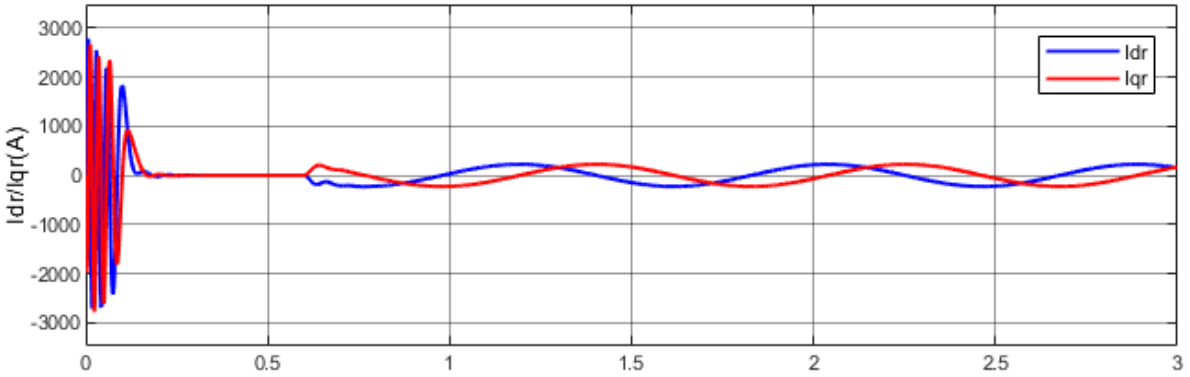
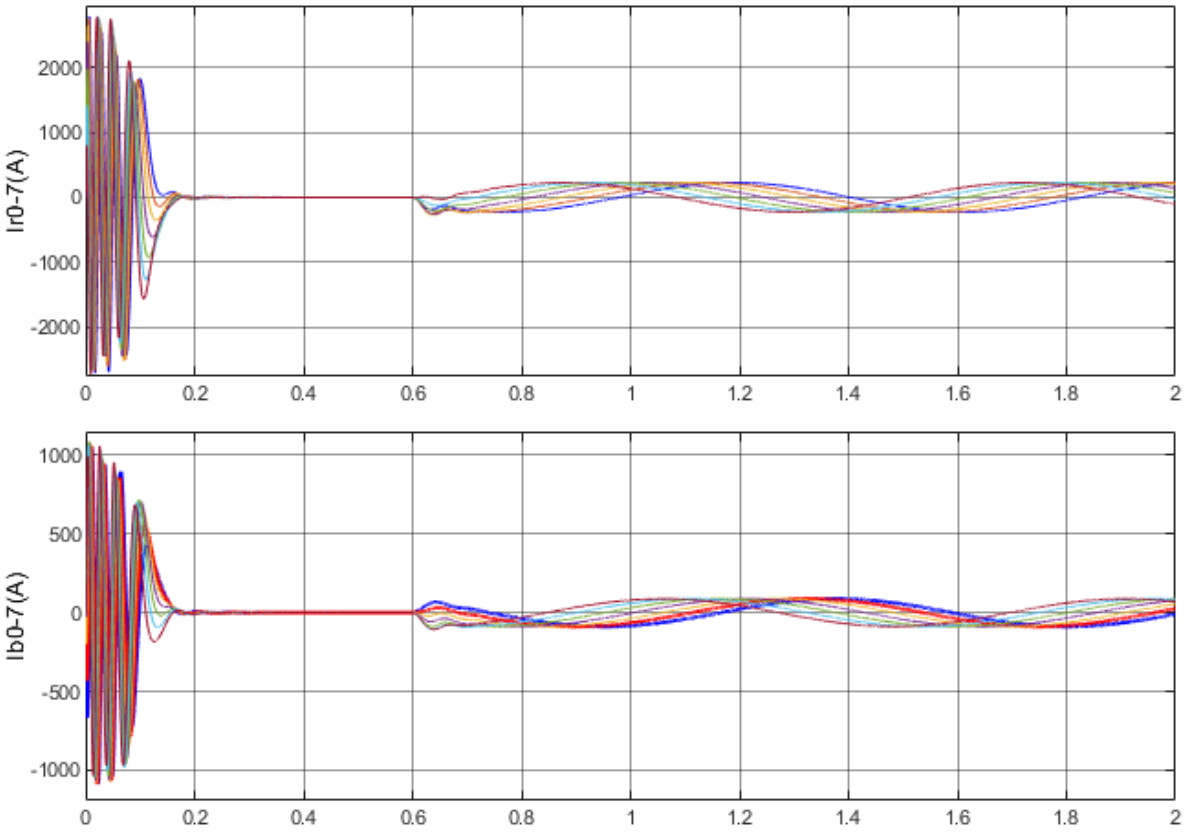


Figure III.22. Phase a current, I_{ds}/I_{qs} and I_{dr}/I_{qr} currents in healthy machine case with load.



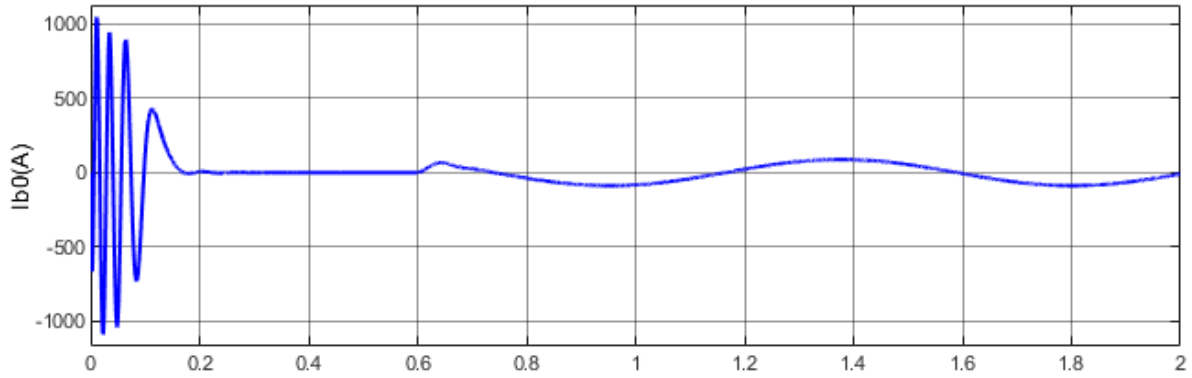


Figure III.23. Current of ring portions 0 to 7, current of bar 0 to 7 and current of bar 0 in healthy machine case with load.

III.4.3 One broken bar:

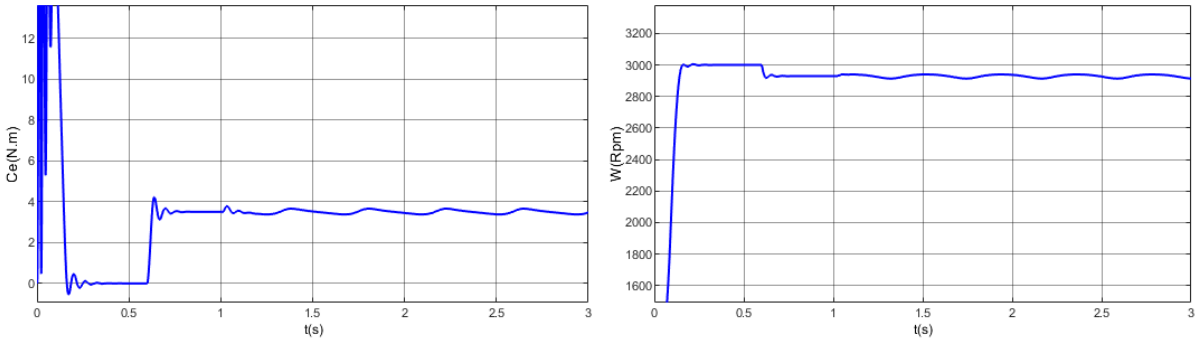
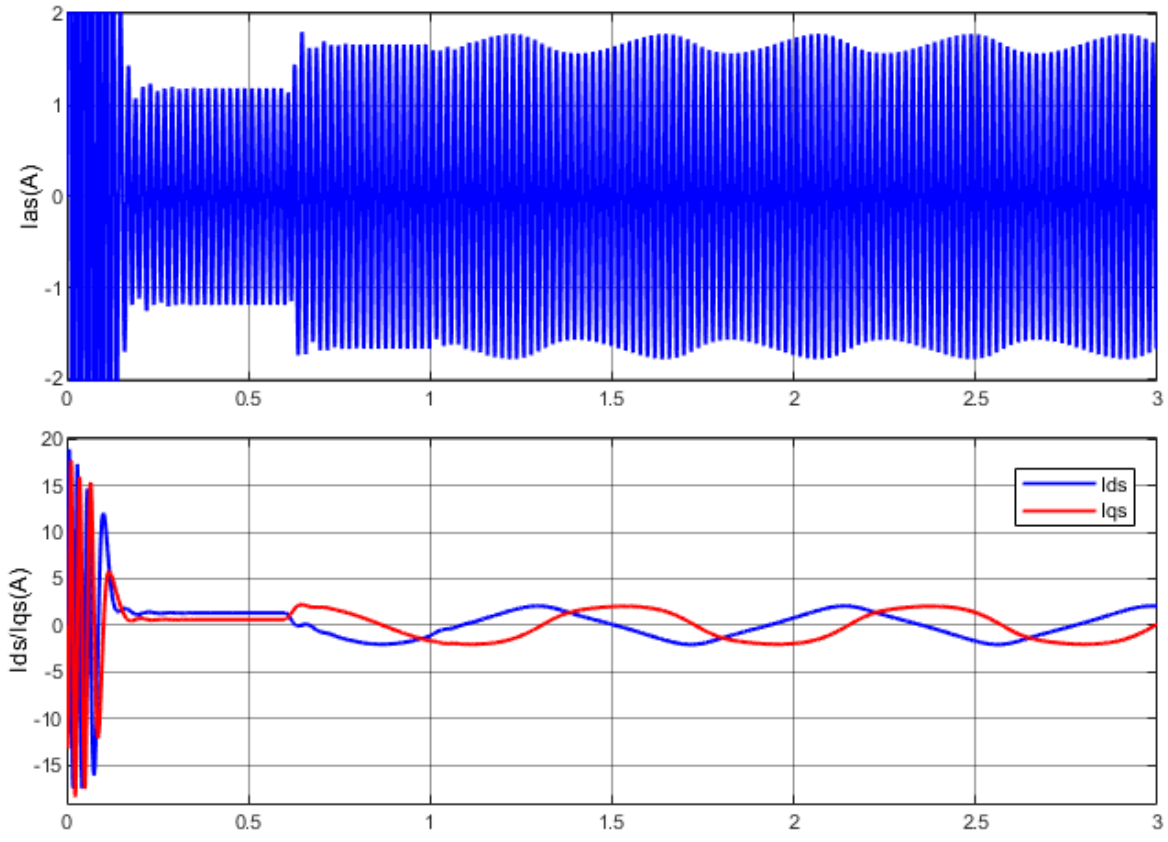


Figure III.24. Electromagnetic torque and rotation speed in one broken bar case.



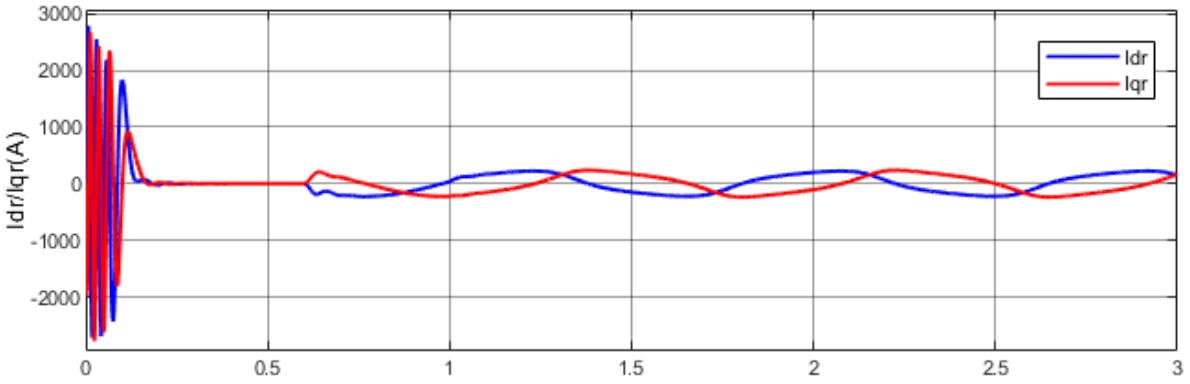


Figure III.25. Phase a current, I_{ds}/I_{qs} and I_{dr}/I_{qr} currents in one broken bar case.

III.4.4 Two adjacent broken bars:

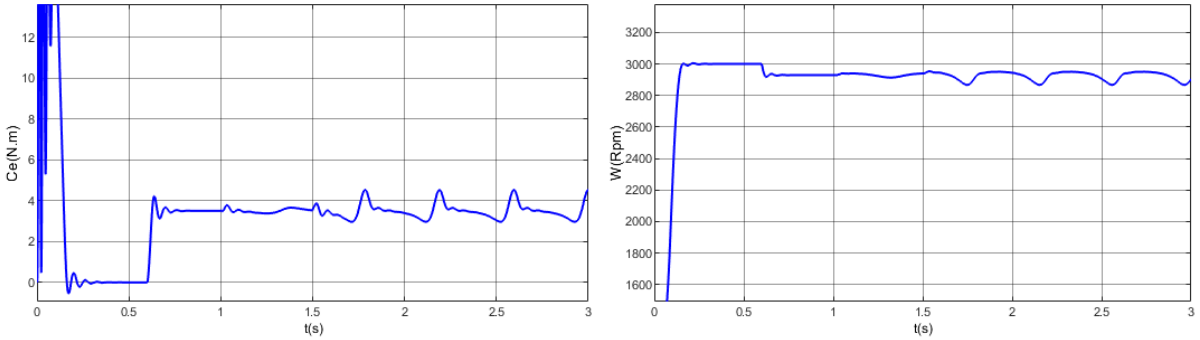
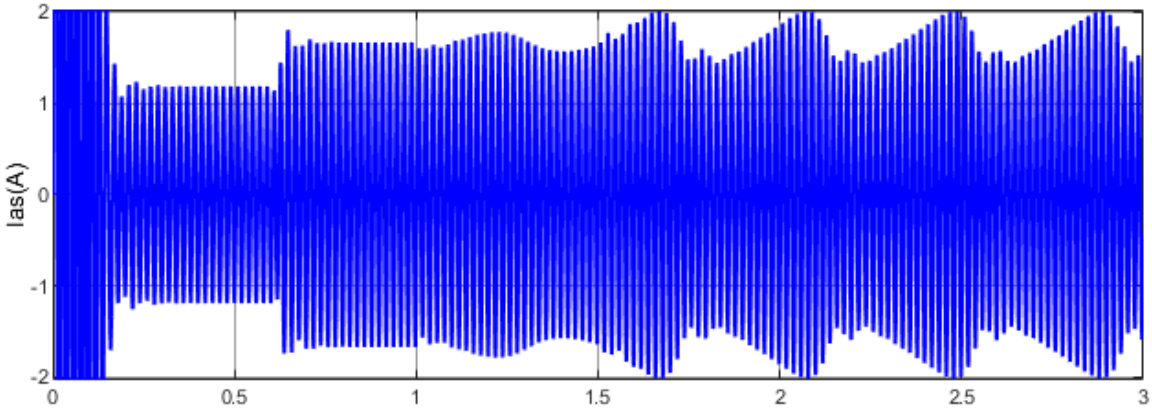


Figure III.26. Electromagnetic torque and rotation speed in two adjacent broken bars case.



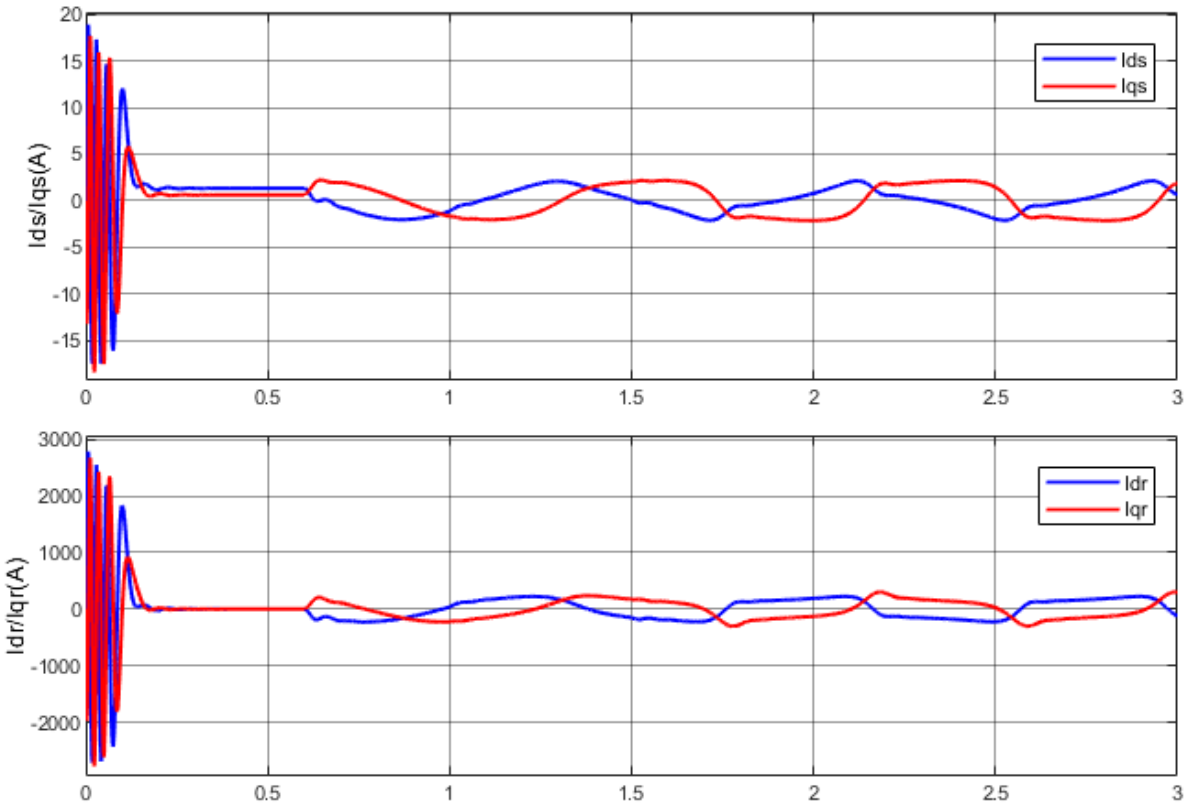


Figure III.27. Phase a current, I_{ds}/I_{qs} and I_{dr}/I_{qr} currents in two adjacent broken bars case.

III.5 Result interpretation (Comparison of the reduced model and the complete model):

The simulation results provide a comprehensive comparison between the complete model and the reduced model, demonstrating their similarities and validating the accuracy of the reduced approach. By analyzing the behavior of rotational speed, electromagnetic torque, stator and rotor currents, and fault-induced oscillations, we can assess the effectiveness of the reduced model in replicating the characteristics of the complete model while maintaining computational efficiency.

III.5.1 No-load operation:

In both models, when the machine operates under no-load conditions, the rotational speed stabilizes near synchronous speed after an initial transient phase. This confirms that the reduced model accurately captures the fundamental dynamic behavior of the induction motor in the absence of external load torque. The electromagnetic torque also stabilizes near zero, which is consistent with theoretical expectations.

Furthermore, the stator currents, I_{ds}/I_{qs}, I_{dr}/I_{qr} and rotor bar currents I_{r0} to I_{r7}, I_{b0} to I_{b7} exhibit small but nonzero values in steady state. This is primarily due to the influence of harmonic fields, which do not rotate precisely at synchronous speed, leading to induced currents in the rotor. The presence of these residual currents is observed in both models, reinforcing the accuracy of the reduced model in representing core electromagnetic interactions. Additionally, since viscous friction is assumed to be zero, it does not generate resistive torque or contribute to rotor bar currents, ensuring consistency between the two models.

III.5.2 Operation under load:

When a load torque of 3.5 N·m is applied, both models show a similar response in terms of speed and torque behavior. The rotational speed stabilizes at 2929 rpm, which aligns with the expected operating conditions under load. Additionally, the electromagnetic torque (C_{em}) in both models stabilizes at 3.5 N·m, accurately balancing the resistive torque.

One key observation is that the oscillations in torque and speed become more pronounced in the presence of faults, but the reduced model successfully captures this effect. This suggests that the simplified mathematical representation maintains the ability to simulate load-induced effects with a high degree of accuracy.

III.5.3 Fault Representation

The models exhibit similar trends in rotor bar and stator current responses when faults occur. The introduction of a bar break at t = 1s (b_0) and an additional break at t = 2s (b_1) leads to notable oscillations in the electromagnetic torque and rotational speed at a frequency of ($2.g.f_s$), as observed in both models. These oscillations grow in amplitude as the number of broken bars increases, a trend that is clearly reflected in the reduced model, demonstrating its ability to replicate fault-induced dynamics.

Additionally, the current redistribution among rotor bars is another critical similarity. When a rotor fault occurs, the currents in the broken bars drop to nearly zero, while the adjacent bars experience increased current flow due to the redistribution of electrical and thermal stresses. The increased amplitude of stator phase currents is also proportional to the number of broken bars, reinforcing the fact that the reduced model effectively captures the fundamental consequences of rotor faults.

III.5.4 Oscillatory effects and harmonic interactions:

A significant finding from the analysis is that both models reveal the interaction between rotor field harmonics and stator winding fields, leading to the emergence of a direct and a reverse field component. This interaction results in an electromagnetic torque composed of a constant component and a sinusoidal component with a pulsation of ($2.g.\omega_s$), which causes speed oscillations. The fact that these oscillatory effects appear in both the complete and reduced models highlights the reduced model's ability to accurately simulate the electromagnetic dynamics of an induction motor.

III.6 Conclusion:

The results demonstrate that the reduced model provides a highly accurate representation of the complete model, capturing key motor characteristics under both no-load and load conditions, as well as in the presence of faults. The steady-state and transient responses in speed, torque, and current distribution are closely aligned in both models, proving that the reduced approach effectively preserves the essential electrical and mechanical dynamics while offering computational efficiency.

Moreover, the fault-induced oscillations and current redistribution effects are well-represented in the reduced model, validating its applicability for simulating rotor faults, harmonic effects, and machine deterioration over time. The ability of the reduced model to replicate these behaviors makes it a powerful tool for fault diagnosis, condition monitoring, and predictive maintenance in induction motors.

The next chapter, we will present the simulation results of spectral analysis for different cases using the reduced model.

Chapter IV: Spectral analysis of stator current

IV.1 Introduction:

To diagnose the broken bar faults in asynchronous machines, multiple analytical approaches are employed, each offering unique advantages:

- Spectral analysis: Examines the frequency spectrum of signals such as stator current and vibration to identify characteristic fault frequencies.
- Cepstral analysis: Detects periodic structures within a signal, making it useful for identifying rotor bar defects.
- Time-frequency and time-scale methods: Techniques such as wavelet transforms and short-time Fourier transform (STFT) provide deeper insights into transient faults by analyzing signals in both time and frequency domains.

IV.2 Spectral analysis approaches:

There are two broad approaches to spectral analysis methods are divided into two main types, non-parametric and parametric Methods, each having their advantages and disadvantages.

IV.2.1 Non-parametric methods:

These methods estimate the power spectral density (PSD) without assuming an underlying model. Examples include:

Periodogram and Correlogram: Traditional techniques for PSD estimation.

Windowing Techniques (e.g., Bartlett, Welch, Blackman-Tukey): Used to enhance frequency resolution by minimizing spectral leakage.

While easy to implement, non-parametric methods often suffer from high variance and limited resolution.

IV.2.2 Parametric methods:

These techniques assume a mathematical model to estimate the power spectrum. Common methods include:

Yule-Walker (Y-W) Equations: Used for estimating autoregressive (AR) model coefficients.

Levinson-Durbin Algorithm: Efficiently solves Y-W equations to improve spectral estimation

Maximum Likelihood (ML) and Burg Algorithms: Provide enhanced accuracy in power spectrum estimation.

Parametric methods offer higher resolution but require careful selection of model parameters [9] [10] [11].

IV.3 Result of spectral analysis:

IV.3.1 Windowing in frequency domain analysis:

When analyzing signals using the Fast Fourier Transform (FFT), one fundamental limitation arises from the assumption that the sampled signal represents exactly one period of a periodic waveform. In practice, this assumption rarely holds true. Instead, signals often comprise a non-integer number of cycles, leading to abrupt discontinuities at the endpoints of the sampled segment. These discontinuities introduce spectral leakage the smearing of signal energy across multiple frequency bins which compromises the fidelity of the frequency domain representation this is illustrated in Figure IV.1, where it can be observed that the sideband frequencies and amplitudes are difficult to distinguish.

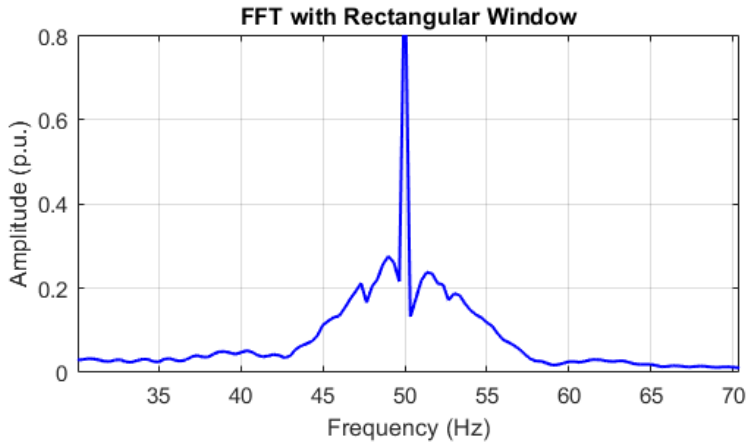


Figure IV.1. Result of spectral analysis of stator current with no windowing one broken bar case at t=1s.

Windowing is a technique developed to address this challenge. The core idea of windowing is to multiply the time-domain signal by a carefully chosen window function that tapers smoothly to zero at the boundaries. This suppresses the artificial discontinuities caused by truncating the signal, thereby reducing spectral leakage in the frequency domain output of the FFT.

Window functions are defined by their main lobe width and side lobe levels. The main lobe determines frequency resolution (how close two frequency components can be while still being distinguishable), whereas the side lobes impact the amount of leakage from nearby frequencies. Thus, selecting an appropriate window requires balancing these competing factors:

- High side lobe roll-off rate windows, like the Hann or Blackman-Harris, are useful for isolating a signal from distant interfering components.
- Low maximum side lobe level windows are preferred when nearby interference is strong.

- A narrow main lobe is ideal for resolving closely spaced frequencies.
- A flat top window provides better amplitude accuracy but at the cost of wider peaks.

Importantly, even using no window (the so-called rectangular or uniform window) constitutes a form of windowing, since the sampling process inherently truncates the signal. This implicit window has a sinc-shaped spectrum, which tends to introduce pronounced side lobes, exacerbating spectral leakage.

Among various options, the Hanning (Hann) window offers a balanced trade-off and is often recommended as a general-purpose window due to its good frequency resolution and reduced leakage. However, no single window is universally optimal, and selection should be guided by the specific characteristics of the signal and the analysis goals [12].

IV.3.2 Result of spectral analysis of stator current with 4 types of windowing, one broken bar case:

To determine the most suitable window for spectral analysis, the case of a single rotor bar break at t=1s is analyzed using different FFT window functions, which is illustrated in Figure IV.2.

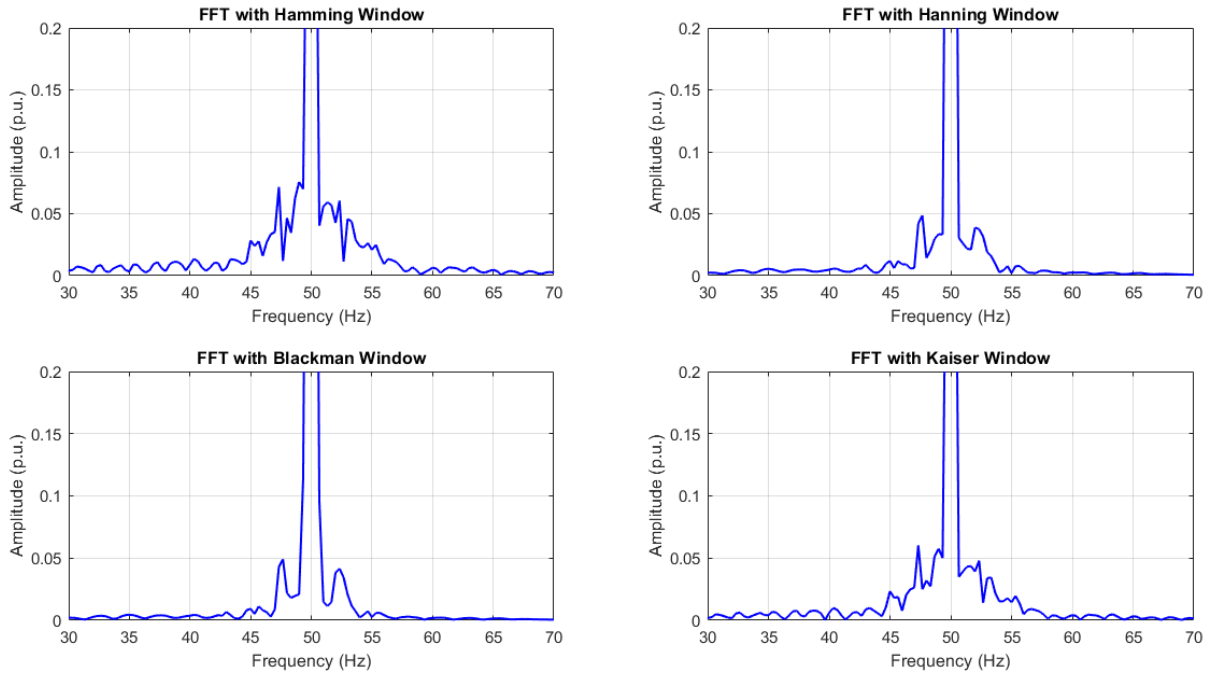


Figure IV.2. Result of spectral analysis of stator current with Hamming, Hanning, Blackman and Kaiser windows.

We observe that Hanning and Blackman provide the best results in reducing spectral leakage, the main difference between the Hanning and Blackman windows lies in the width of the resulting spectral lines those from the Hanning window are broader. This indicates that the

Hanning window is more effective at highlighting spectral lines that help in detecting rotor faults. Therefore, spectral analysis of the stator current is performed using the Hanning window.

IV.3.3 Result of spectral analysis of stator current with Hanning Window, healthy machine case:

During the simulation of a healthy motor, no major sidebands are observed, as illustrated in Figure IV.3.

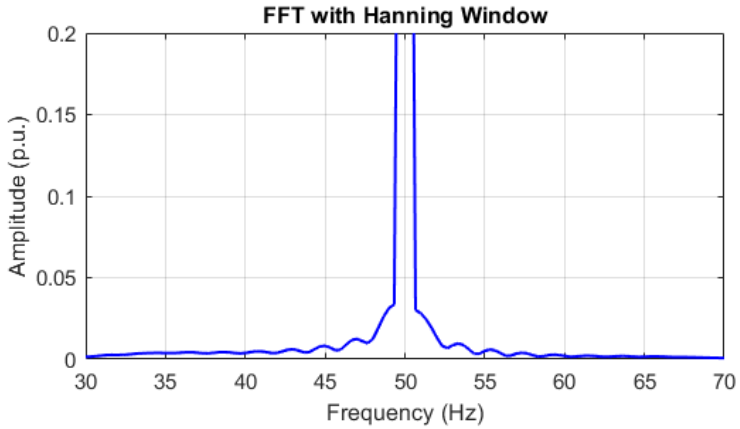


Figure IV.3. Result of spectral analysis of stator current with Hanning Window, healthy machine case.

The minor sidebands result from the sudden load change from 0 to 3.5 Nm at t = 0.6 s. These sidebands do not appear in Figure IV.4, where the same load (corresponding to a 2.3% slip) is applied from the start.

IV.3.4 Result of spectral analysis to study the effect of load:

In this case the motor starts directly with a load with no abrupt load change.

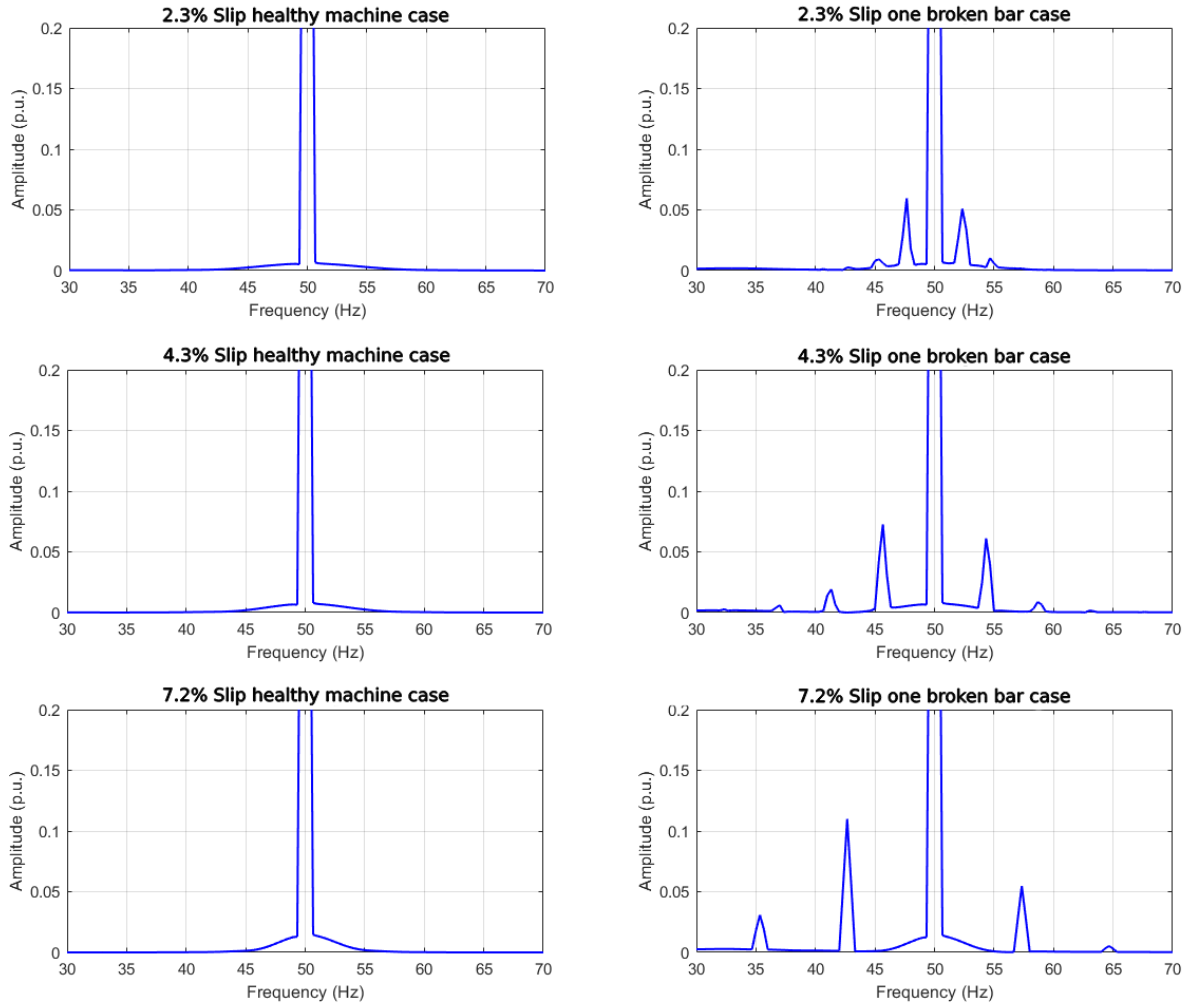


Figure IV.4. Result of spectral analysis of 2.3%, 4.3% and 7.2% for both healthy and one broken bar case.

The FFT spectrum reveal distinct differences as slip increases. For healthy machines, the fundamental peak at 50 Hz remains dominant across all slip values (2.3%, 4.3%, and 7.2%), with no major sidebands forming. In contrast, for the case of one broken bar, sidebands emerge at ~47.7 Hz and ~52.3 Hz for 2.3% slip, corresponding to the characteristic broken bar signature, which can be described by the formula $(1\pm2g)f_s$. As slip increases, the amplitude of these sidebands rises significantly as well as their frequency. By 7.2% slip, the sidebands are more pronounced and widely spaced, reflecting the dependence on slip. Additionally, higher-order sidebands, such as $(1\pm4g)f_s$ and $(1\pm6g)f_s$, start to appear at higher slip values, further indicating the presence of the rotor fault.

IV.3.5 Result of spectral analysis to study the effect of position and number of broken bars:

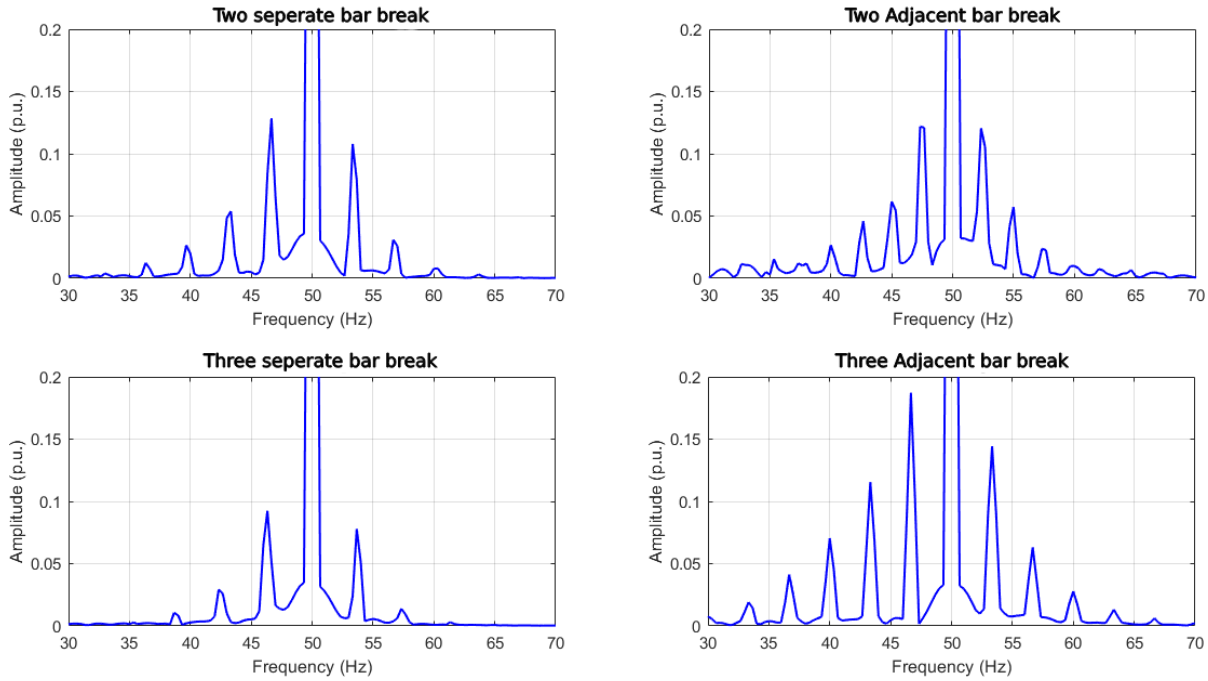


Figure IV.5. Result of spectral analysis of adjacent and separate bar breaks in both two-bar and three-bar break cases.

In the case of two spatially separated broken bars (b_0 and b_{10}), the FFT spectrum reveals a clear peak at 50 Hz, accompanied by moderate sidebands around $(1\pm2g)f_s$ as well as small sidebands at $(1\pm4g)f_s$ and $(1\pm6g)f_s$. These are characteristic of the harmonic components associated with rotor asymmetry and correspond to expected sideband frequencies arising from the slip in the machine. The amplitudes in this configuration remain relatively low, indicating that the magnetic imbalance is partially mitigated due to the spatial distribution of the faults. Because the broken bars are not concentrated in a single region, their opposing effects on the magnetic field can partially cancel each other out, resulting in weaker fault signatures.

When the two broken bars are positioned adjacently (b_0 and b_1), the spectral characteristics change notably. While the sideband frequencies remain similar, their amplitudes increase significantly. This is due to the concentrated asymmetry caused by the localized nature of the fault, which enhances the disruption of the magnetic field. Consequently, the current modulation is more pronounced, and the sidebands in the spectrum are amplified, reflecting a more severe mechanical and electrical disturbance in the rotor system.

In the three separate broken bar case (b_0, b_5 and b_{11}), although the number of faults has increased compared to the two-bar cases, the sideband amplitudes are not significantly higher and even

lower in $(1\pm4g)f_s$ and $(1\pm6g)f_s$ frequency than those observed with two adjacent breaks. This can be attributed to the symmetrical or more evenly spaced distribution of the broken bars. When rotor faults are positioned in a more balanced configuration around the circumference of the rotor, their individual contributions to the magnetic asymmetry tend to cancel out to some extent. This symmetry reduces the net distortion in the air-gap flux, which in turn lowers the amplitude of the sidebands despite the increased number of faults. Thus, the overall severity of the spectral signature may appear less intense than in the two adjacent bar case, illustrating how fault placement influences the diagnosis as much as fault quantity which can be shown more clearly in Figure IV.6.

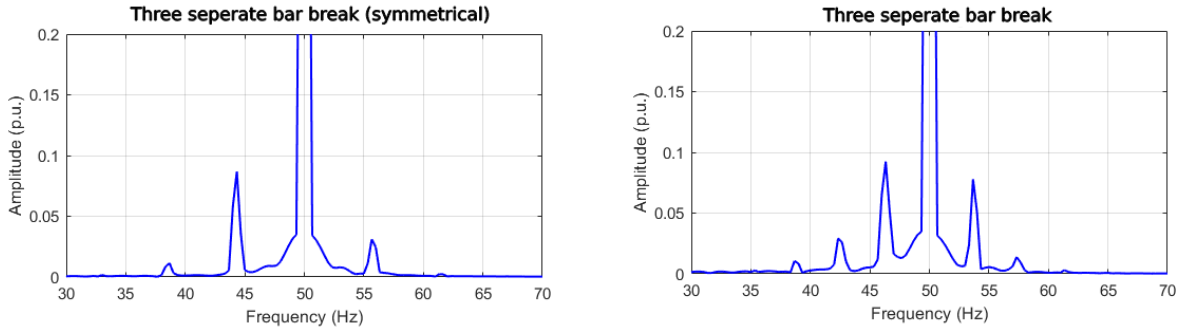


Figure IV.6. Result of spectral analysis of evenly and non-evenly separate bar breaks.

The most severe spectral characteristics are observed in the three adjacent broken bar case. This configuration presents the highest sideband amplitudes, almost reaching 0.2 per unit, and displays additional harmonic components beyond the immediate vicinity of the fundamental frequency. The close proximity of the three faults leads to a concentrated and unbalanced rotor field, causing substantial current and torque oscillations. The FFT spectrum in this case is not only more intense but also more complex, reflecting the combined effects of harmonic distortion and higher-order slip harmonics.

IV.4 Conclusion:

This chapter demonstrated the effectiveness of spectral analysis techniques in diagnosing faults in squirrel cage induction motors, specifically focusing on broken rotor bars. Both non-parametric and parametric methods were explored, with a particular emphasis on the application of windowing functions to improve the accuracy of frequency domain analysis. Among the windowing techniques applied, the Hanning window exhibited a balanced trade-off between main lobe width and side lobe attenuation, proving effective in isolating characteristic fault frequencies.

The spectral characteristics of stator current signals under various conditions healthy, single-bar broken, multi-bar broken, and under different load scenarios were thoroughly analyzed. The results confirmed that fault-induced frequency components become increasingly pronounced with both load intensity and the severity of rotor damage. Additionally, the study highlighted the influence of fault location and symmetry, as spectral signatures varied with the spatial arrangement of the broken bars.

Finally, this chapter confirmed that spectral analysis is a powerful diagnostic tool, capable of detecting subtle variations in the motor's operational profile. When integrated with accurate modeling and simulation as established in the previous chapters it offers a reliable foundation for condition monitoring and predictive maintenance of induction motors. This analytical framework will serve as a stepping stone toward the development of intelligent diagnostic systems, especially when fused with machine learning techniques in future research

General conclusion

This thesis presented a comprehensive framework for fault diagnosis in squirrel cage induction motors, encompassing theoretical modeling, simulation, and advanced signal analysis. Beginning with a foundational overview of induction motor structure and common fault types both mechanical and electrical Chapter I laid the groundwork for understanding the operational vulnerabilities of these critical machines. Emphasis was placed on early fault detection, given its importance in minimizing downtime and preserving industrial system integrity.

Building upon this foundation, Chapter II introduced a mathematically rigorous model of the induction motor using the magnetically coupled electric circuits method. This model incorporated both stator and rotor dynamics, including the possibility of rotor bar and end ring faults, allowing for precise simulation of electromechanical behavior. The reduced model, developed through the application of transformation techniques, offered a more tractable system for analytical and computational purposes while maintaining essential dynamic characteristics.

In Chapter III, the developed models were simulated under various operating conditions—no-load, load, and multiple fault scenarios. The simulation results validated the robustness of the model and its capability to replicate the effects of rotor faults on system performance, including torque, speed, and current characteristics. Comparisons between the complete and reduced models confirmed the latter's efficacy in capturing fault-induced phenomena with reduced computational complexity.

Finally, Chapter IV explored the application of spectral analysis techniques for result interpretation, particularly focusing on stator current signal analysis. By applying both non-parametric and parametric spectral methods, it was shown that characteristic fault frequencies could be reliably extracted under varying load and fault conditions. The implementation of windowing functions such as Hanning and Hamming further enhanced frequency resolution, aiding in the clear identification of fault signatures. These findings demonstrated the value of spectral analysis as a complementary tool to the physical and simulation-based diagnostic approaches introduced earlier.

In conclusion, this work successfully bridges the gap between theoretical modeling and practical diagnostics, offering a unified approach to induction motor fault detection. The integration of analytical modeling, simulation, and spectral signal processing provides a solid platform for future development of intelligent condition monitoring systems. Future work could build upon the present findings by integrating real-time data acquisition systems, advanced fault classification using machine learning algorithms, and adaptive control strategies tailored for predictive maintenance. A promising perspective for this research also includes the

development of intelligent control architectures and the application of artificial intelligence (AI)-based techniques for enhanced diagnostic accuracy and the precise identification of electrical and/or mechanical fault types. These approaches can significantly improve system reliability, fault tolerance, and autonomous decision-making capabilities in complex electromechanical systems.

Annex

Nominal power (P): 1.1 kW

Nominal line voltage (V): 220 V

Supply frequency (fs): 50 Hz

Number of pole pairs (p): 1

Average radius of the air gap (R): 35.76 mm

Length of the magnetic circuit (L): 65 mm

Air gap thickness (e): 0.2 mm

Number of rotor bars (Nr): 16

Number of stator turns per phase (Ns): 160

Stator winding resistance (Rs): 7.58 Ω

Rotor bar resistance (Rr): 150 μΩ

Short-circuit ring resistance (Re): 72 μΩ

Short-circuit ring total inductance (Le): 0.1 μH

Inductance of a rotor bar (Lb): 0.1 μH

Stator leakage inductance (Lfs): 26.5 mH

Friction coefficient (Kf): 0

Moment of inertia (J): 0.006093 kg·m²

Bibliography

[1] S. Meradi, "Estimation des paramètres et des états de la machine asynchrone en vue de diagnostic des défauts rotoriques," University of Mohamed Khider Biskra, Department Of Electrotechnics, 2007.

[2] S. BELHAMDI, «Prise en compte d'un défaut rotorique dans la commande d'un moteur asynchrone,» University of Mohamed Khider Biskra, Department Of Electrotechnics, 2005.

[3] "mechdaily," [Online]. Available: https://www.mechdaily.com/what-is-electric-motor/. [Accessed 25 March 2025].

[4] G. Didier, modélisation et diagnostic de la machine asynchrone en présence de défaillances, Thèse de doctorat, Université Henri Poincaré - Nancy, 2004.

[5] M. Blodt, P. Granjon, B. Raison and G. Rostaing, "Models for Bearing Damage Detection in Induction Motors Using Stator Current Monitoring," IEEE International Symposium on Industrial Electronics (ISIE 2004), France, 2004.

[6] R. Casimir, "Diagnostic des défauts des machines asynchrones par reconnaissance des formes," The Centrale Lyon, 2007.

[7] R. M. B, Rotating Machinery: Practical Solutions to Unbalance and Misalignment, The Fairmont Press, Inc., 2004.

[8] M. Belacel, S. Rahali and A. Saci, "Simulation Des Machines Asynchrones à Cage Modèle Multi-enroulements Dédiée Au Diagnostic Des Défauts," University Of M'sila Faculty Of Sciences And Engineering Sciences, Department Of Electrotechnics, 2007.

[9] H. Zhao and L. Gui, "Nonparametric and parametric methods of spectral analysis," Department of Information Science and Electronic Engineering, Zhejiang University, Key Laboratory of Ocean Observation-Imaging, 2019.

[10] A. V. Oppenheim and R. W. Schafer, Discrete-Time Signal Processing THIRD EDITION, Pearson Higher Education, 2010.

[11] P. Stoica and M. Randolph, "SPECTRAL ANALYSIS OF SIGNALS," PRENTICE HAL, 2005.

[12] National Instruments, "Instrument Fundamentals with NI," [Online]. Available: https://www.ni.com/en/forms/instrument-fundamentals-complete-guide.html. [Accessed 16 May 2025].

[13] R. Abdessemed, modélisation et simulation des machines électriques, Paris: editions ellipses, 2011.

[14] L. Noureddine, "Diagnostic de défauts au rotor d'une," University of Laghouat, Department of Electrical Engineering, 2005.

[15] J. P. Hautier and J. P. Caron, Modélisation et commande de la machine asynchrone, Paris: Editions Technip, 1995.

[16] F. Gianluca, "SUPERVISION AND DIAGNOSIS OF INDUSTRIAL SYSTEMS," University of Cagliari, 2017.

[17] H. TALHAOUI, "Contrôle par Mode Glissant d'une Machine Asynchrone en tenant Compte des Défauts," Université Mohamed Khider – Biskra, Faculté des Sciences et de la technologie, Département Génie Electrique, 2011.

[18] N. BESSOUS, M. M. REZAOUI, I. MERZOUK, A. BORNI and L. ZAROUR, "Analyse détaillée du contenu spectral dans le courant statorique des machines asynchrones sous un défaut de la cassure de barres rotoriques en utilisant la technique de la MCSA-FFT," R E C U E I L D E M É C A N I Q U E, 2019.